A high-order finite volume method with improved isotherms reconstruction for the computation of multiphase flows using the Navier-Stokes-Korteweg equations

Abel Martínez[a], Luis Ramírez[a], Xesús Nogueira[a,*], Sofiane Khelladi[b], Fermín Navarrina[a]

[a]*Group of Numerical Methods in Engineering, Universidade da Coruña, Campus de Elviña, 15071, A Coruña, Spain*
[b]*Laboratoire de Dynamique des Fluides, Arts et Métiers ParisTech, 151 Boulevard de l'Hôpital. 75013 Paris, France.*

Abstract

In this work we solve the Navier-Stokes-Korteweg (NSK) equations to simulate a two-phase fluid with phase change. We use these equations on a diffuse interface approach, where the properties of the fluid vary continuously across the interface that separates the different phases. The model is able to describe the behavior of both phases with the same set of equations, and it is also able to handle problems with great changes in the topology of the problem. However, high-order derivatives are present in NSK equations, which is a difficulty for the design of a numerical method to solve the problem. Here, we propose the use of a high-order Finite Volume method with Moving Least Squares approximations to handle high-order derivatives and solve the NSK equations. Moreover, a new methodology to obtain accurate equations of state is presented. In this method, we use any accurate equation of state for

---

*Corresponding author, e-mail: xesus.nogueira@udc.es

the pure phases. Under the saturation curve, a B-spline reconstruction fulfilling a given set of thermodynamic criteria is performed. The new EOS can be used for computations using diffuse interface modeling. Several numerical examples to show the accuracy of the new approach are presented.

1. Introduction

Phase change and coexistence between two phases of the same substance in the same space are phenomena which often takes place in engineering. Multiphase flow simulation is currently an area of extensive research, in which great progress has been made recently.

Sharp-interface and diffuse-interface models are the two mayor branches in multiphase flow modeling. The first ones [1, 2, 3] simulate different phases of the fluid as separated, therefore in the contact region between phases (known as the interface) a discontinuity in the properties of the fluid is produced. The interaction between different phases is achieved by imposing balance equations as boundary conditions in the interface, which has to be solved at the same time that the system of partial differential equations. As the interface is able to displace, the numerical simulation needs algorithms to track its position each time step.

Diffuse-interface models, or phase-field models [4, 5, 6, 7], represent a different approach. These models establish that in the interface there is a smooth and continuous transition between the properties of each phase, and therefore it has non-zero thickness. The first advantage is that diffuse

interface modeling has solid foundations in thermodynamics and statistical mechanics. Moreover, in these methods the interface is part of the solution of the governing equations, thus the same system of equations can be applied to the entire domain, avoiding expensive algorithms for tracking the interface and being capable of reproducing numerically problems with large topological changes. The main problem of diffuse-interface models is that the governing equations are highly non-lineal, and to be realistic the interface must be extremely thin, so they require very fine meshes or adaptive mesh techniques.

One mathematical model to simulate multiphase flow is the Navier-Stokes-Korteweg model (NSK), which is a highly non-lineal system belonging to the diffuse interface models type. One drawback of this model is the third-order partial-differential equations that appear in the formulation [8], difficult to implement numerically.

In literature we find some numerical solutions of the Navier-Stokes Korteweg equations. The Finite Difference method (FD) has been successfully used to solve the NSK system [9]. However, it has limitations for its use in complex geometries, which are commonly found in engineering. To overcome this limitation, other approaches have been proposed to compute the NSK system using the Discontinuous Galerkin method [10, 11, 12, 13] or Isogeometric analysis [14]. In this work, we propose a high-order Finite Volume method based on Moving Least Square approximations (FV-MLS) for the resolution of the NSK system on unstructured grids [15, 16, 17, 18, 19]. Moving Least Squares (MLS) [20] approximations are used for the calculation of the gradients and successive derivatives required for the reconstruction of the variables inside each control volume, an interpolation technique widely

3

used in *meshfree* methods [21, 22, 23].

In diffuse interface modeling, a single equation of state (EOS) is required to describe the thermodynamic properties of the different phases that appear in the problem. The most commonly used equation which reproduce phase change between two different states of matter is the van der Waals equation of state [24, 25]. Although this equation of state is accurate enough for a great number of substances, it is very inaccurate for the case of water. In this work, we also propose a new algorithm to obtain new accurate equations of state suitable for diffuse interface modeling. This is achieved by using more accurate equations to represent the different phases of the substance and creating new expressions to ensure a continuous transition between the pure phases.

The outline of this paper is as follows: First of all, the numerical method is presented. Then, we show a new method to obtain accurate equations of states. Finally, a few numerical results are presented in Section 4, and then, conclusions are drawn.

2. Numerical method

2.1. Navier-Stokes-Korteweg equations

The isothermal Navier-Stokes Korteweg (NSK) equations, can be written in non-dimensional form [26] as system of conservation laws as

$$\frac{\partial \boldsymbol{u}}{\partial t} + \boldsymbol{\nabla} \cdot \left(\boldsymbol{\mathcal{F}}^{\mathcal{H}} - \boldsymbol{\mathcal{F}}^{\mathcal{E}} - \boldsymbol{\mathcal{F}}^{\mathcal{K}} \right) = \boldsymbol{0}$$

where $\boldsymbol{u}$ is the vector of variables, $\boldsymbol{\mathcal{F}}^{\mathcal{H}}$ is the inviscid flux vector, $\boldsymbol{\mathcal{F}}^{\mathcal{E}}$ is the viscous flux vector and $\boldsymbol{\mathcal{F}}^{\mathcal{K}}$ is the Korteweg flux vector.

$$\boldsymbol{u} = \left\{ \begin{array}{c} \widehat{\rho} \\ \widehat{\rho}\widehat{v_x} \\ \widehat{\rho}\widehat{v_y} \end{array} \right\}$$

$$\boldsymbol{\mathcal{F}}_x^{\mathcal{H}} = \begin{pmatrix} \widehat{\rho}\widehat{v_x} \\ \widehat{\rho}\widehat{v_x}^2 + \widehat{P} \\ \widehat{\rho}\widehat{v_x}\widehat{v_y} \end{pmatrix}, \quad \boldsymbol{\mathcal{F}}_y^{\mathcal{H}} = \begin{pmatrix} \widehat{\rho}\widehat{v_y} \\ \widehat{\rho}\widehat{v_x}\widehat{v_y} \\ \widehat{\rho}\widehat{v_y}^2 + \widehat{P} \end{pmatrix}$$

$$\boldsymbol{\mathcal{F}}_x^{\mathcal{E}} = \frac{1}{Re} \begin{pmatrix} 0 \\ 2\partial_x\widehat{v_x} - \frac{2}{3}\left(\partial_x\widehat{v_x} + \partial_y\widehat{v_y}\right) \\ \left(\partial_y\widehat{v_x} + \partial_x\widehat{v_y}\right) \end{pmatrix}, \boldsymbol{\mathcal{F}}_y^{\mathcal{E}} = \frac{1}{Re} \begin{pmatrix} 0 \\ \left(\partial_y\widehat{v_x} + \partial_x\widehat{v_y}\right) \\ 2\partial_y\widehat{v_y} - \frac{2}{3}\widehat{\mu}\left(\partial_x\widehat{v_x} + \partial_y\widehat{v_y}\right) \end{pmatrix}$$

$$\boldsymbol{\mathcal{F}}_x^{\mathcal{K}} = \frac{1}{We} \begin{pmatrix} 0 \\ \left(\widehat{\rho}\Delta\widehat{\rho} + \frac{1}{2}|\nabla\widehat{\rho}|^2 - \partial_x\widehat{\rho}\partial_x\widehat{\rho}\right) \\ -\left(\partial_x\widehat{\rho}\partial_y\widehat{\rho}\right) \end{pmatrix}, \boldsymbol{\mathcal{F}}_y^{\mathcal{K}} = \frac{1}{We} \begin{pmatrix} 0 \\ -\left(\partial_y\widehat{\rho}\partial_x\widehat{\rho}\right) \\ \left(\rho\Delta\widehat{\rho} + \frac{1}{2}|\nabla\widehat{\rho}|^2 - \partial_y\widehat{\rho}\partial_y\widehat{\rho}\right) \end{pmatrix}$$

where $\widehat{\rho}$ is the dimensionless density, $\widehat{P}$ is the dimensionless pressure and $\widehat{\boldsymbol{v}} = (\widehat{v_x}, \widehat{v_y})^T$ the dimensionless velocity field. The Reynolds number, Re, and the Weber number, We can be expressed in terms of the dimensionless dynamic viscosity $\widehat{\mu}$ and the dimensionless capillarity coefficient $\widehat{\lambda}$ as

$$Re = \frac{1}{\widehat{\mu}} \qquad\qquad We = \frac{1}{\widehat{\lambda}}$$

2.2. The FV-MLS method

2.2.1. Finite Volume formulation

In this work, we propose a discretization of the NSK equations described in (1) using the FV-MLS method [15, 16, 17, 18, 19]. We start with the

integral form of the system of conservation laws for each control volume I

$$\int_{\Omega_I} \frac{\partial \boldsymbol{u}}{\partial t}\, d\Omega + \int_{\Gamma_I} \left(\boldsymbol{\mathcal{F}}^{\mathcal{H}} - \boldsymbol{\mathcal{F}}^{\mathcal{E}} - \boldsymbol{\mathcal{F}}^{\mathcal{K}} \right) \cdot \boldsymbol{n}\, d\Gamma = \boldsymbol{0} \tag{1}$$

where Ω_I is the control volume area, Γ_I is the control volume boundary and $\boldsymbol{n} = (n_x, n_y)^T$ is the unitary exterior normal of the contour of Ω_I. Moreover, $\boldsymbol{\mathcal{F}}^{\mathcal{H}}, \boldsymbol{\mathcal{F}}^{\mathcal{E}}, \boldsymbol{\mathcal{F}}^{\mathcal{K}}$ are the convective, diffusive and Korteweg fluxes, respectively. Note that the integral over Γ_I is performed over the interfaces (edges in 2D or faces in 3D) between two adjacent control volumes. In order to increase the order of accuracy of a FV scheme there is a need to reconstruct the variable $\boldsymbol{u}$ at the integration points on the interface. For convective terms, this is usually achieved by using Taylor's polynomials [15, 16, 17, 18, 19]. The reconstruction for diffusive and Korteweg terms will be discussed later.

We define a reference point (*node*), $\boldsymbol{x}_I$ inside each cell (the cell centroid). The spatial representation of the solution is as follows: consider a function $\boldsymbol{u}(\boldsymbol{x})$, given by its point values, $\boldsymbol{u}_I = \boldsymbol{u}(\boldsymbol{x}_I)$, at the cell centroids, with coordinates $\boldsymbol{x}_I$. The approximate function $\boldsymbol{u}^h(\boldsymbol{x})$ belongs to the subspace spanned by a set of *basis functions* $\{\Phi_I(\boldsymbol{x})\}$ associated to the nodes, such that $\boldsymbol{u}^h(\boldsymbol{x})$ is given by

$$\boldsymbol{u}^h(\boldsymbol{x}) = \sum_{j=1}^{n_{\boldsymbol{x}}} \Phi_j(\boldsymbol{x}) \boldsymbol{u}_j \tag{2}$$

which states that the approximation at a point $\boldsymbol{x}$ is computed using certain $n_{\boldsymbol{x}}$ surrounding nodes. This set of nodes is referred to as the *stencil* associated to the evaluation point $\boldsymbol{x}$, and $\boldsymbol{u}_j$ refers to the value of the function at the points of the stencil. The number of nodes of the stencil depends on the order of the reconstruction, and will be discussed later.

Introducing the component-wise reconstructed function $\boldsymbol{u}^h$ in equation

6

(1) we obtain

$$\int_{\Omega_I} \frac{\partial \boldsymbol{u}^h}{\partial t} \, d\Omega + \int_{\Gamma_I} \left(\boldsymbol{\mathcal{F}}^{h\mathcal{H}} - \boldsymbol{\mathcal{F}}^{h\mathcal{E}} - \boldsymbol{\mathcal{F}}^{h\mathcal{K}} \right) \cdot \boldsymbol{n} \, d\Gamma = \boldsymbol{0} \tag{3}$$

where the superindex h indicates that the flux is computed with the reconstructed function $\boldsymbol{u}^h$.

2.2.2. Moving Least Squares approximations

In equation (2) $\Phi_j(\boldsymbol{x})$ are the MLS shape functions. Here we only introduce a brief description of the computation of MLS functions, and we refer the reader to [15, 16, 17, 18, 19] for a complete description of the procedure. To compute the MLS shape functions we define an m-dimensional basis, which in this case is defined as $\boldsymbol{p}^T(\boldsymbol{x}) = (1, x, y, x^2, y^2, xy, ...) \in \mathbb{R}^m$. The dimension of the basis, m, determines the minimum number of points of the stencil. However, for stability reasons, this minimum number should be increased. In this work we use a polynomial cubic basis, with a value of $n_{\boldsymbol{x}} = 13$ for convective fluxes and $n_{\boldsymbol{x}} = 16$ for the diffusive fluxes. Then, the MLS-shape functions are defined as

$$\boldsymbol{\Phi}^T(\boldsymbol{x}) = \boldsymbol{p}^T(\boldsymbol{x}) \boldsymbol{M}^{-1} \boldsymbol{P} \boldsymbol{W}(\boldsymbol{x})$$

where $P_{ij} = [\boldsymbol{p}^T(\boldsymbol{x}_j)]_i$, is a $m \times n_{\boldsymbol{x}}$ matrix where the basis functions are evaluated at each point of the stencil, and $\boldsymbol{M}$ is the $m \times m$ moment matrix given by

$$\boldsymbol{M} = \boldsymbol{P} \boldsymbol{W} \boldsymbol{P}^T$$

The kernel function $\boldsymbol{W}$ determines the properties of the scheme, required in the computation of $\boldsymbol{\Phi}^T(\boldsymbol{x})$. We have chosen to use an exponential kernel [19], defined as

$$W_i(\boldsymbol{x}_j) = \frac{e^{-\left(\frac{s}{c}\right)^2} - e^{-\left(\frac{d_m}{c}\right)^2}}{1 - e^{-\left(\frac{d_m}{c}\right)^2}}$$

with $s = |\boldsymbol{x}_j - \boldsymbol{x}_i|$, $d_m = max\left(|\boldsymbol{x}_j - \boldsymbol{x}_i|\right)$, with $j = 1, \ldots, n_{x^*}$, $c = \frac{d_m}{2\kappa}$, and κ is a shape parameter, which in this work is taken as $\kappa = 3$. Moreover, x_i refers to the position of the point where the MLS shape function is evaluated.

Using MLS reconstructions we obtain a continuous surface (volume in 3D) with the value of the reconstructed function. This surface/volume is defined on a support given by the stencil of the approximation. Thus, from this surface/volume it is possible to define a single value of the reconstructed function at integration points, and this is the procedure used here for diffusive and Korteweg fluxes. For the convective flux, we use a different procedure to allow using the Riemann solver technology. For convective fluxes we *"break"* the MLS reconstruction to obtain the two Riemann states at the interface by using Taylor series expansions, as explained in the following section.

2.2.3. Convective fluxes

For hyperbolic fluxes, we introduce a *"broken"* reconstruction in terms of Taylor series, which approximates $\boldsymbol{u}(\boldsymbol{x})$ locally inside each cell I, and is discontinuous across cell interfaces. This procedure allows us to calculate the numerical flux at each Gauss point at cell interfaces by using a Riemann solver. In general, we require the order of accuracy of the broken reconstruction to be the same as that of the original continuous reconstruction. Thus,

using Taylor series expansions; a quadratic reconstruction inside cell I, reads

$$\boldsymbol{u}_I^{hb}(\boldsymbol{x}) = \boldsymbol{u}_I^h + \boldsymbol{\nabla}\boldsymbol{u}_I^h \cdot (\boldsymbol{x} - \boldsymbol{x}_I) + \frac{1}{2}(\boldsymbol{x} - \boldsymbol{x}_I)^T \boldsymbol{H}^h (\boldsymbol{x} - \boldsymbol{x}_I) \tag{4}$$

where the gradient $\boldsymbol{\nabla}\boldsymbol{u}_I^h$ and the Hessian matrix $\boldsymbol{H}^h$ involve the successive derivatives of the continuous reconstruction $\boldsymbol{u}^h(\boldsymbol{x})$, which are evaluated at the cell centroids using MLS.

For unsteady problems, additional terms must be introduced in equation (4) to enforce conservation of the mean

$$\frac{1}{V_I}\int_{\boldsymbol{x}\in\Omega_I}\boldsymbol{u}(\boldsymbol{x})d\Omega = \boldsymbol{u}_I$$

where V_I is the measure of the control volume cell.

Thus, the quadratic reconstruction for unsteady problems reads as

$$\begin{aligned}\boldsymbol{u}(\boldsymbol{x}) \quad = \quad & \boldsymbol{u}_I + \boldsymbol{\nabla}\boldsymbol{u}_I \cdot (\boldsymbol{x} - \boldsymbol{x}_I) + \tfrac{1}{2}(\boldsymbol{x} - \boldsymbol{x}_I)^T \boldsymbol{H}_I(\boldsymbol{x} - \boldsymbol{x}_I) - \\[2mm] & - \frac{1}{2V_I}\left[I_{xx}\frac{\partial^2\boldsymbol{u}}{\partial x^2} + 2I_{xy}\frac{\partial^2\boldsymbol{u}}{\partial x\partial y} + I_{yy}\frac{\partial^2\boldsymbol{u}}{\partial y^2}\right]\end{aligned}$$

with

$$I_{xx} = \int_\Omega(x - x_I)^2 d\Omega, \quad I_{yy} = \int_\Omega(y - y_I)^2 d\Omega$$

$$I_{xy} = \int_\Omega(x - x_I)(y - y_I)d\Omega$$

In this work, we have used the Rusanov Riemann solver [27] with the Li and Gu's fix for all speed flows [28], which can be written as

$$\boldsymbol{\Theta}_{i+\frac{1}{2}} = \frac{1}{2}(\boldsymbol{\mathcal{F}}^{hH+} + \boldsymbol{\mathcal{F}}^{hH-}) \cdot \boldsymbol{n} - \frac{1}{2}S^+\Delta^*(\boldsymbol{u}) \tag{5}$$

with

$$S^+ = max(|\boldsymbol{v}^+| + c^+, |\boldsymbol{v}^-| + c^-) \tag{6}$$

We define $\Delta^*(\boldsymbol{u})$ as follows

$$\Delta^*(\boldsymbol{u}) = \left\{ \begin{array}{c} \widehat{\rho}^{hb+} - \widehat{\rho}^{hb-} \\ f(M_l)\left((\widehat{\rho v_x})^{hb+} - (\widehat{\rho v_x})^{hb-}\right) \\ f(M_l)\left((\widehat{\rho v_y})^{hb+} - (\widehat{\rho v_y})^{hb-}\right) \end{array} \right\}$$

where

$$f(M_l) = \begin{cases} \min(M_l, 1), & \text{if } \dfrac{\partial \widehat{P}}{\partial \widehat{\rho}} > 0 \\ 0, & \text{if } \dfrac{\partial \widehat{P}}{\partial \widehat{\rho}} \leq 0 \end{cases} \tag{7}$$

and

$$M_l = \frac{|\widehat{v}_x|_I + |\widehat{v}_y|_I}{c_I}$$

Note that the Li and Gu's fix is simply obtained by multiplying the momentum difference term in the momentum equations by the function $f(M_l)$. In equation (6) c_I is the sound velocity on the cell I and $|\boldsymbol{v}|$ is the modulus of the velocity vector at integration point and $\Delta(\boldsymbol{u}) = (\boldsymbol{u}^{hb+} - \boldsymbol{u}^{hb-})$. In interface regions, the sound velocity may become a complex number. In particular, this happens when $\frac{\partial \widehat{P}}{\partial \widehat{\rho}}$ is negative. Thus, we define c_I as follows

$$c_I = \sqrt{\max\left(\frac{\partial \widehat{P}}{\partial \widehat{\rho}}, 0\right)} \tag{8}$$

Note that the use of Li and Gu's fix allows to use this scheme in the interface region, where the equations are no longer hyperbolic. Then, introducing equation (5) in equation (3)

$$\int_{\Omega_I} \frac{\partial \boldsymbol{u}^h}{\partial t}\, d\Omega + \int_{\Gamma_I} \boldsymbol{\Theta}(\boldsymbol{u}^{hb+}, \boldsymbol{u}^{hb-})\, d\Gamma - \int_{\Gamma_I} \left(\boldsymbol{\mathcal{F}}^{h\mathcal{E}} - \boldsymbol{\mathcal{F}}^{h\mathcal{K}}\right) \cdot \boldsymbol{n}\, d\Gamma = \boldsymbol{0}$$

10

Note that this dual continuous/discontinuous (for diffusive/Korteweg and convective terms) reconstruction of the solution is crucial in order to obtain accurate and efficient numerical schemes for mixed parabolic/hyperbolic problems. The cell-wise broken reconstruction defined here is actually a piecewise continuous approximation to $\boldsymbol{u}^h$. As commented previously, the advantage is that it allows to make use of Riemann solvers, and other standard finite volume technologies, while keeping some consistency in terms of functional representation.

2.2.4. Diffusive and Korteweg fluxes

For elliptic fluxes a continuous reconstruction is used with MLS directly at cell interfaces. The numerical method proposed in this work, performs a centered, direct evaluation of the viscous fluxes at the quadrature points on the edges using information from neighboring cells, through the use of MLS approximations. Thus, focusing on the Navier–Stokes-Korteweg equations, the evaluation of the diffusive and Korteweg fluxes requires interpolating the derivatives of the dimensionless density and velocity vector $\widehat{\boldsymbol{v}} = (\widehat{v_x}, \widehat{v_y})^T$ at each quadrature point $\boldsymbol{x}_{iq}$. Using MLS approximations, these values are readily computed as

$$\partial_{x_i}\widehat{\rho} = \sum_{j=1}^{n_{\boldsymbol{x}}} \partial_{x_i}\Phi_j(\boldsymbol{x}_{iq})\widehat{\rho}_j \tag{9}$$

$$\begin{aligned}
\partial_{x_i}\widehat{v_x} &= \sum_{j=1}^{n_{\boldsymbol{x}}} \partial_{x_i}\Phi_j(\boldsymbol{x}_{iq})\widehat{v}_{xj} \\
\partial_{x_i}\widehat{v_y} &= \sum_{j=1}^{n_{\boldsymbol{x}}} \partial_{x_i}\Phi_j(\boldsymbol{x}_{iq})\widehat{v}_{yj}
\end{aligned} \tag{10}$$

Note that in equations (9) and (10) the derivatives of the MLS shape

function are computed at the quadrature point $\boldsymbol{x}_{iq}$. We refer the reader to [15, 16, 17, 18, 19] for a complete description of the procedure of the computation of derivatives of MLS shape functions.

In all the MLS approximations of this work, we have used a cubic polynomial basis, which leads to third-order discretizations of the first derivatives [29].

2.2.5. Pure Reconstruction test

In order to demonstrate the accuracy and the formal order of reconstruction of the variables and its derivatives, we perform a reconstruction test case. The 2D square domain $\Omega = [-1.0, 1.0] \times [-1.0, 1.0]$ is discretized with a set of structured meshes. We define the function to be reconstructed as

$$f(\boldsymbol{r}) = a \, e^{-\frac{|\boldsymbol{r}|^2}{2b}} \tag{11}$$

where $\boldsymbol{r}$ is the radial distance $\boldsymbol{r} = \sqrt{(x - 0.5)^2 + (y - 0.5)^2}$, $a = 1/(\sqrt{2b\pi})$ and $b = 0.20$. First, we set the known value of the function to each cell centroid. Next, MLS reconstruction and first, second and third derivatives of the function are computed at each integration point. Then, since the analytical values are known the L_2^N for the reconstruction and derivatives errors for each mesh resolution is computed. Finally, once the errors are known, the convergence rates are computed as

$$O^N = \frac{\log\left(L_2^{N_1}/L_2^{N_2}\right)}{\log(\sqrt{N_2/N_1})}. \tag{12}$$

where N_1 and N_2 are the number of control volumes for two different mesh resolution. L_2^N is define as the L_2-norm of the error on the mesh with N control volumes. L_2 error norms and convergence rates of the reconstructed

function and its first, second and third derivatives, are plotted in Figure 1 for a cubic reconstruction. It is shown that the expected convergence rates are recovered.
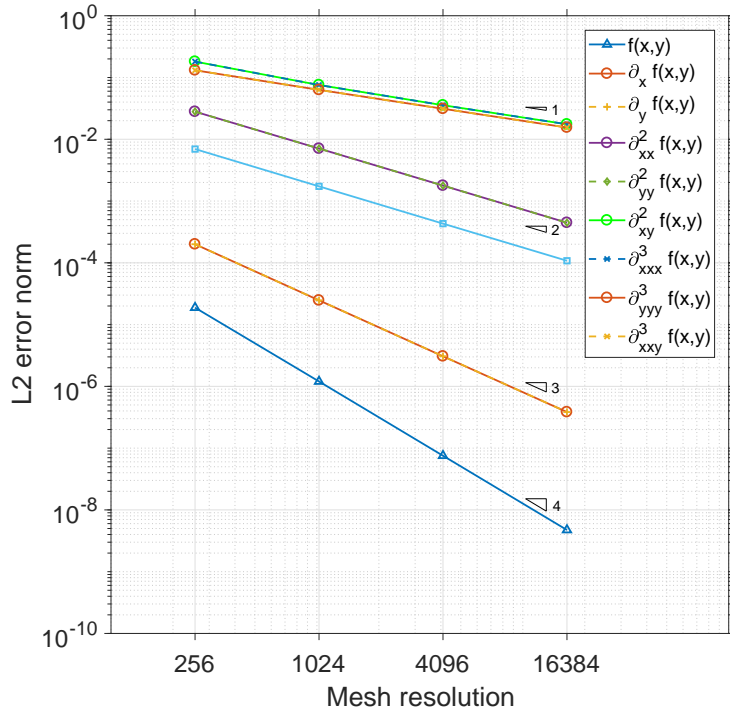

Figure 1: 2D Reconstruction test cases using a cubic MLS reconstrucion. L_2^N error norms and convergence rates of the reconstructed function and its first, second and third derivatives.

3. A new Equation of State

In order to fully define the Navier-Stokes Korteweg system, it has to be complemented with a non-monotone equation of state of pressure with density. Traditionally, the most commonly used is the van der Waals equation of state (vdW EOS) [24], which reads in non-dimensional form as

$$\widehat{P} = \frac{8\widehat{T}\widehat{\rho}}{27(1-\widehat{\rho})} - \widehat{\rho}^2$$

with

$$\widehat{T} = \frac{T}{T_{crit}} = \frac{27R}{8ab}T \qquad \widehat{P} = \frac{1}{ab^2}P \qquad \widehat{\rho} = \frac{1}{b}\rho$$

where R is the ideal gas constant and the parameters a and b are constants that have different values for each substance.
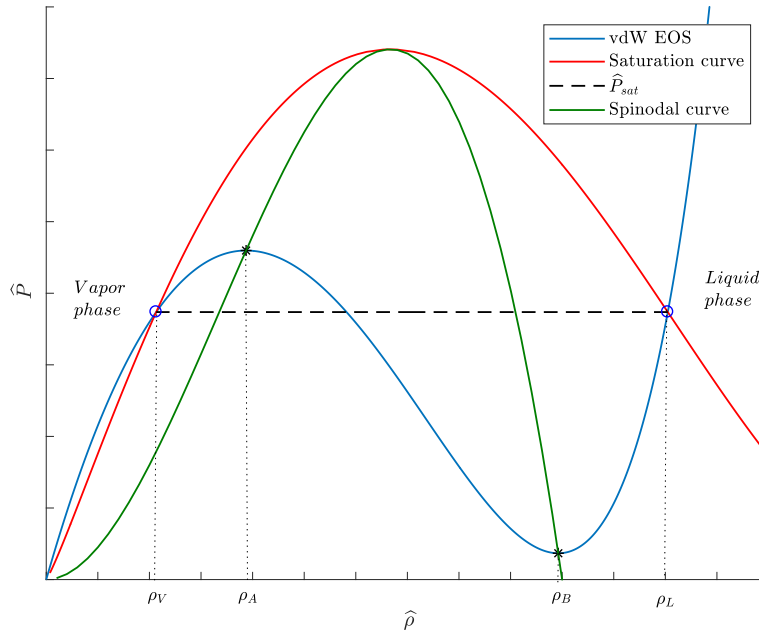
Figure 2: Van der Waals isotherm corresponding to $\widehat{T} = 0.85$. In the figure we show the pure phases outside the saturation curve, vapor phase on the left and liquid phase on the right. Inside the spinodal curve, $\frac{\partial \widehat{P}}{\partial \widehat{\rho}} < 0$ and therefore the EOS is of elliptic type. Between both curves, the metastable regions take place.

In figure 2 we plot the van der Waals equation for water at $\widehat{T} = 0.85$.

14

Under the critical temperature ($\widehat{T} < 1$), the pressure function for a van der Waals fluid is non-monotone with density, unlike in a one-phase fluid. The function represented can be interpreted as a vapor phase in the range $(0, \widehat{\rho}_A)$ and a liquid phase in the range $(\widehat{\rho}_B, 1)$. As it can be seen in figure 2, under the spinodal curve between $\widehat{\rho}_A$ and $\widehat{\rho}_B$ the curve is of elliptic type as $\frac{\partial \widehat{P}}{\partial \widehat{\rho}} < 0$. In this region a decrease in the pressure of the substance corresponds to an increase in the density, which represents a non-physical behavior.

The saturation curve in figure 2 separates two different stable phases (pure phases), the vapor pure phase on the left and the liquid pure phase on the right. The saturation curve represents the region where the thermodynamic equilibrium between both phases takes place, and thus they can coexist at the same time. Inside the saturation curve, the van der Waals equation of state proposes a continuous and smooth transition between both phases, which makes it adequate for diffuse interface modeling. The expression inside the saturation curve, though, does not represent a physical behavior, it is not possible to obtain the real value in a laboratory and therefore there is not empirical data to compare with.

Nevertheless, van der Waals equation of state, although accurate for a great number of substances, does not reproduce precisely the specific case of water. There are certainly other equations of state meant to adjust better to empirical data, such as the Modified Tait's equation [30, 31], written in equation (13), which represents the liquid phase of the water.

$$\widehat{P} = K_0 \left[\left(\frac{\widehat{\rho}}{\widehat{\rho}_{l,sat}(T)} \right)^N - 1 \right] + \widehat{P}_{sat}(T) \tag{13}$$

where N, K_0, $\widehat{\rho}_{l,sat}$ and $\widehat{P}_{sat}$ are known parameters which are tabulated

for a certain temperature.

However, due to the absence of experimental data, more precise equations of state do not establish any expression for the substance under the saturation curve. Hence, their use is not valid in a diffuse-interface model.

In figure 3, we present the isotherms at $\widehat{T} = 0.85$ using the van der Waals and Tait EOS compared with the experimental data obtained from the NIST database [32]. Figure 3 shows the inaccuracy problems that van der Waals EOS present in pure phases outside the saturation curve, which are even greater as the temperature drops. Moreover, the van der Waals equation states that the thermodynamic equilibrium between phases is produced at the saturation pressure $\widehat{P} = vdW\widehat{P}_{sat}$, which does not match with the real value $\widehat{P} = \widehat{P}_{sat}$. For the temperature used in figure 3 ($\widehat{T} = 0.85$), the value of $vdW\widehat{P}_{sat}$ has a relative error of 82.03%.

3.1. Objective and main ideas

In this work we propose a new algorithm to obtain more accurate equations of state from data exclusively in the pure phases. In our approach, the global EOS is defined by blending two different EOS that reproduce accurately both of the pure phases. Here, we specifically address the case of water, and we use Tait's EOS for the liquid phase and van der Waals EOS for the vapor phase. In order to be adequate for diffuse interface modeling, the global equation of state must also describe the behavior of the fluid under the saturation curve. This is achieved by creating a reconstruction of the equation as it is explained in the following paragraphs. A first approach to the problem addressed in this work is exposed in [33], where the author proposes different expressions of the isotherms under the saturation curve.
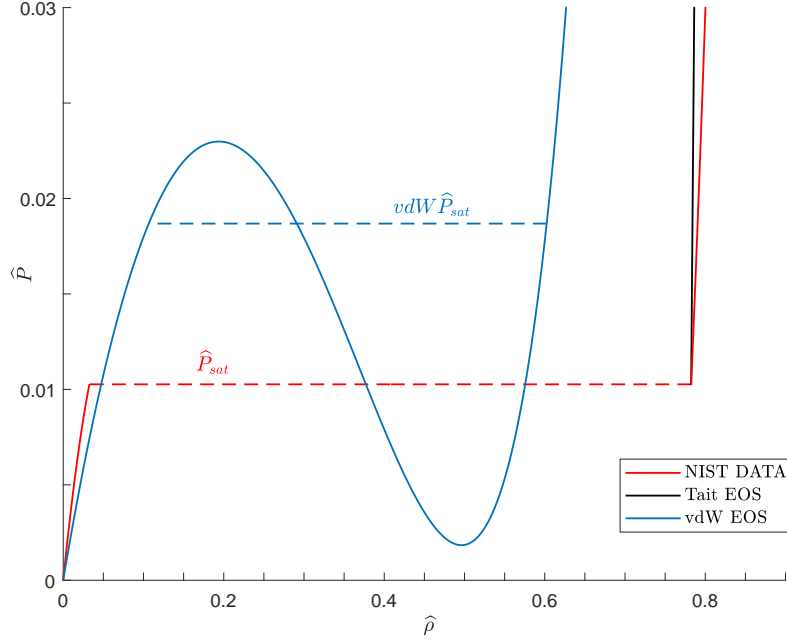
Figure 3: Comparison of the isotherms (at $\widehat{T} = 0.85$) using the van der Waals and Tait EOS for water, compared with the experimental data obtained from the NIST database.

With the aim of creating the global EOS, some requirements have to be verified, which can be listed as

1. In the global EOS, both the function and the first derivative must be continuous (the EOS must be at least of differentiability class C^1), as it is required for the discretization of the Korteweg tensor and to ensure the continuity of the sound velocity. The reconstruction will be performed between the points $\widehat{\rho}_V$ and $\widehat{\rho}_L$, both with the same pressure $\widehat{P}_{sat}$ (figure 3) which are defined by the equations of state used in the pure phases.

2. Additionally, the expression under the saturation curve must be defined in such a way that the thermodynamic equilibrium is produced at the saturation points, at density $\widehat{\rho}_V$ for the vapor phase and $\widehat{\rho}_L$ for the liquid phase, both with the same pressure $\widehat{P}_{sat}$ (figure 2). In this work, this is achieved by fulfilling the Maxwell equal area rule [34], which states that Gibbs free energy has the same value in two phases in equilibrium [35]. However, there are other possibilities, since there is some controversy about the use of the Maxwell rule [34]. For the isothermal case, the Gibbs free energy reads as

$$G = PV - \int PdV + \varphi(T)$$

where $P = P(V)$, which under the saturation curve can be modified according to the reconstruction used.

Minimum values in Gibbs free energy function represent the thermodynamic equilibrium of the substance [36]. In a one-component system with two phases at equilibrium, for a certain value of temperature and pressure the Gibbs free energy for both phases must be equal. In figure 4 (a) we show for $\widehat{T} = 0.85$ and $\widehat{P} = 0.187$ a representation of the Gibbs free energy for the van der Waals equation as a function of the volume $\widehat{v} = 1/\widehat{\rho}$. For this combination of temperature and pressure, the Gibbs free energy function produces two minima with the same value, representing two phases at equilibrium at $\widehat{v} = \widehat{v}_L$ and $\widehat{v} = \widehat{v}_V$, which are the volume values of the saturation points. Moreover, in figure 4 (b) we plot the van der Waals equation of state as function of the volume. From a geometrical point of view, the Maxwell rule can be interpreted as the condition in which the two regions delimited by

18

$\widehat{P}_{sat}$ have the same area in the representation of pressure as function of the volume, as it is shown in the two shaded areas in figure 4 (b).
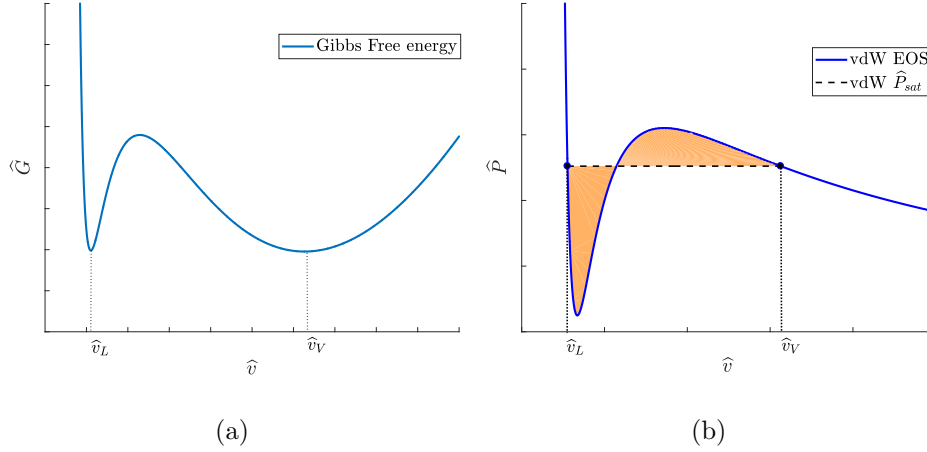

(a)   (b)

Figure 4: In (a), we show a representation of the dimensionless Gibbs free energy depending on $\widehat{v}$ with $\widehat{T} = 0.85$ and $\widehat{P} = 0.187$, which produces two minima with the same free energy value. The figure shows the state of a substance in which both liquid and vapor phases are stable and therefore the coexistence is produced. In (b), we plot the van der Waals equation of state depending on the volume, in which the two shaded areas delimited by $\widehat{P}_{sat} = 0.187$ are equal according to the Maxwell rule.

3. Generally, the reconstruction curve must keep the same shape of the van der Waals equation of state, producing only two points with zero derivative inside the saturation curve, which are the spinodal points. We will elude the creation of new points with zero derivative so as to avoid changes in the shape of the Gibbs free energy (see figure 4), which is directly related to the mechanism of separation of the phases.

Note that the choice of the EOS under the saturation curve, between liquid and vapor phases, will inevitably affect the underlying physics of the

substance within the interface, specifically, it will affect the predicted value of the surface tension, which is related to the excess of the Gibbs free energy inside the interface. Previous works have addressed the modification of the EOS under the saturation curve [33, 37]. In particular, in [37] the authors present a very exhaustive analysis of the thermodynamic effects of modifying the equation of state under the saturation curve in the context of NSK equations. How the expression under the saturation curve affects key variables in the numerical method presented here will be discussed in Section 4.

3.2. Reconstruction function

In order to define the reconstruction function, we use a B-spline approximation due to the great control it provides over the final shape of the curve. In this work, B-splines are computed using the recursive Cox-de Boor algorithm [38]. The blending curve $\overline{S}$ is defined as the sum of B-spline functions of order p $(N_{i,p}(\xi))$ multiplied by a vector-valued constants $\overline{C}_i$, called control points as

$$\overline{S}(\xi) = \sum_{i=1}^{n} N_{i,p}(\xi)\overline{C}_i$$

where n is the number of B-spline shape functions ($\boldsymbol{N}$) and points used in the interpolation.

To meet the continuity and derivability requirements of the EOS curve, the shape functions must be at least quadratic ($p \geq 2$) so that $N_{i,p}(\xi) \in C^{p-1}$. To build the reconstruction we use $n = 6$ control points. Figure 5 shows schematically the kind of curve that we obtain for the EOS under the saturation curve.
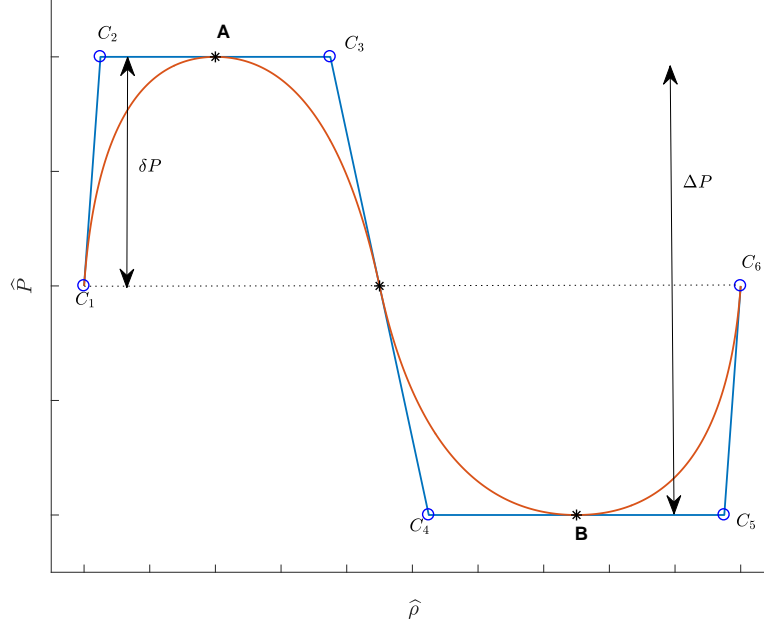
Figure 5: Sketch of the curve obtained for the EOS under the saturation curve using the proposed reconstruction scheme. In the figure, C_i are the control points of the B-Spline and δP and ΔP are parameters of the reconstruction. A and B are the spinodal points of the EOS, which are coincident with the maximum and minimum of the B-Spline curve.

The proposed procedure is summarized as follows

1. Control points C_1 and C_6 are placed at the saturation points, as they are the beginning and the end of the reconstruction domain.

2. The position of the control points C_2 and C_5 determines the value of the initial and final slopes of the curve respectively ($S'(\widehat{\rho}_V) = \alpha_V$ for vapor and $S'(\widehat{\rho}_L) = \alpha_L$ for the liquid phase) as it is seen in figure 5. In order to achieve continuity of the first derivative in the global EOS, these points will be placed to match $\frac{\partial \widehat{P}}{\partial \widehat{\rho}}$ derivatives at the saturation

21

points of the reconstruction curve with those of the pure EOS.

3. The reconstruction curve $\overline{S}$ is tangent to the line segments $\overline{C_2C_3}$, $\overline{C_3C_4}$ and $\overline{C_4C_5}$ in their midpoints (marked in figure 5). Since we set the points C_2 & C_3 and C_4 & C_5 to have the same ordinate value, two of the tangent points have zero derivative, thus they are spinodal points (A and B in figure 5). The density value of the spinodal points (denoted as $\widehat{\rho}_A$ and $\widehat{\rho}_B$) is considered as a given data, and it is chosen so that the general shape of the global EOS is similar to the van der Waals EOS, as it is our reference. Therefore, we keep the same proportional relation between $\widehat{\rho}_V$, $\widehat{\rho}_A$, $\widehat{\rho}_B$ and $\widehat{\rho}_L$ as in vdW EOS.

To completely define the position of the spinodal points, we establish as variables the differences of pressure between the points C_1 and C_2, which we call δP, and the difference of pressure between spinodal points, which we call ΔP, as we show in figure 5. At this point, for a certain value of δP and ΔP we have already established the points C_2 and C_5, as their pressure is known ($\widehat{P}_{sat} + \delta P$ for C_2 and $\widehat{P}_{sat} + \delta P - \Delta P$ for C_4) and they belong to the tangent lines of the EOS at the saturation points.

4. Finally, C_3 and C_4 are chosen such as the midpoints of the line segments $\overline{C_2C_3}$ and $\overline{C_4C_5}$ coincide with the spinodal points. This condition can be expressed as $\overline{C_2A} = \overline{AC_3}$ and $\overline{C_4B} = \overline{BC_5}$.

Thus, in brief, the pair $\left\{ \begin{array}{c} \widehat{\rho} \\ \widehat{P} \end{array} \right\}$ for each control point is given by

$$\overline{C}_1 = \left\{ \begin{array}{c} \widehat{\rho}_V \\ \widehat{P}_{sat} \end{array} \right\} \qquad \overline{C}_2 = \left\{ \begin{array}{c} \widehat{\rho}_V + \frac{\delta P}{\alpha_V} \\ \widehat{P}_{sat} + \delta P \end{array} \right\} \qquad \overline{C}_3 = \left\{ \begin{array}{c} 2\widehat{\rho}_A - (\widehat{\rho}_V + \frac{\delta P}{\alpha_V}) \\ \widehat{P}_{sat} + \delta P \end{array} \right\}$$

$$\overline{C}_4 = \left\{ \begin{array}{c} 2\widehat{\rho}_B - (\widehat{\rho}_L - \frac{\Delta P - \delta P}{\alpha_L}) \\ \widehat{P}_{sat} + \delta P - \Delta P \end{array} \right\} \qquad \overline{C}_5 = \left\{ \begin{array}{c} \widehat{\rho}_L - \frac{\Delta P - \delta P}{\alpha_L} \\ \widehat{P}_{sat} + \delta P - \Delta P \end{array} \right\} \qquad \overline{C}_6 = \left\{ \begin{array}{c} \widehat{\rho}_L \\ \widehat{P}_{sat} \end{array} \right\}$$

$$(14)$$

The position of the control points depends on two parameters, ΔP and δP. In order to completely define the global EOS we keep ΔP as a free parameter, which allow us to have control on the final shape of the reconstruction. The choice of this parameter will affect important thermodynamic properties of the substance, such as the surface tension or the width of the interface.

The value of δP is computed to fulfill the Maxwell's equal area rule, which is expressed in equation (15).

$$\int_{\widehat{v}_L}^{\widehat{v}_V} (\widehat{P}(\widehat{v}) - \widehat{P}_{sat}) d\widehat{v} = 0 \qquad (15)$$

In equation (15), $\widehat{P}(\widehat{v})$ is obtained through the equation of state, which is dependent on the volume $\widehat{v} = 1/\widehat{\rho}$. Moreover, $\widehat{v}_V$ and $\widehat{v}_L$ are the values of the volume at saturation points.

Expanding equation (15) with the values of the control points in the previous expressions (14), results in an analytic expression of δP depending on ΔP, and therefore the curve is completely defined. How ΔP affects the stability and numerical solution of the model will be analyzed in Section 4.

A major advantage in using this algorithm is the great control it provides on the final curve and the simplicity of its application. B-Splines allow us to easily define the initial and final slopes necessary to meet the smoothness requirementsand the position of the zero derivative points. The proposed

23

reconstruction procedure allows us to use different equations of state for each substance and make them suitable for diffuse interface modeling. An additional advantage of the proposed approach is that the reconstruction curve is completely defined by an analytic algorithm.

In figures 6-9 two examples of the equation of state obtained using this algorithm are shown. In the first example, the temperature is set at $\widehat{T} = 0.85$ and $\Delta P = 0.010$. Moreover, in figure 7 the same EOS as a function of the volume (instead of the density) is plotted. In this last figure, it can be seen that the Maxwell equal area rule is fulfilled.

In the second example, shown in figure 8, the equation of state obtained for the temperature $\widehat{T} = 0.65$ and $\Delta P = 0.010$ is drawn. The same EOS as a function of the volume is also shown in figure 9. In this case we use a logarithm scale for the representation of the volume due to the large values of this variable.

4. Numerical results

In this section, several numerical examples are presented to show the ability of the proposed method to simulate two-phase flow phenomena. The numerical examples are computed on a square-shaped computational domain $\Omega = [0, 1] \times [0, 1]$, in which we impose periodic boundary conditions in all directions. For the examples the physical parameters Ca, We and Re are defined as follows

$$Ca = \frac{h^2}{L_0^2} \qquad We = \frac{1}{Ca} \qquad Re = 2\sqrt{We} \qquad L_0 = 1 \quad (16)$$
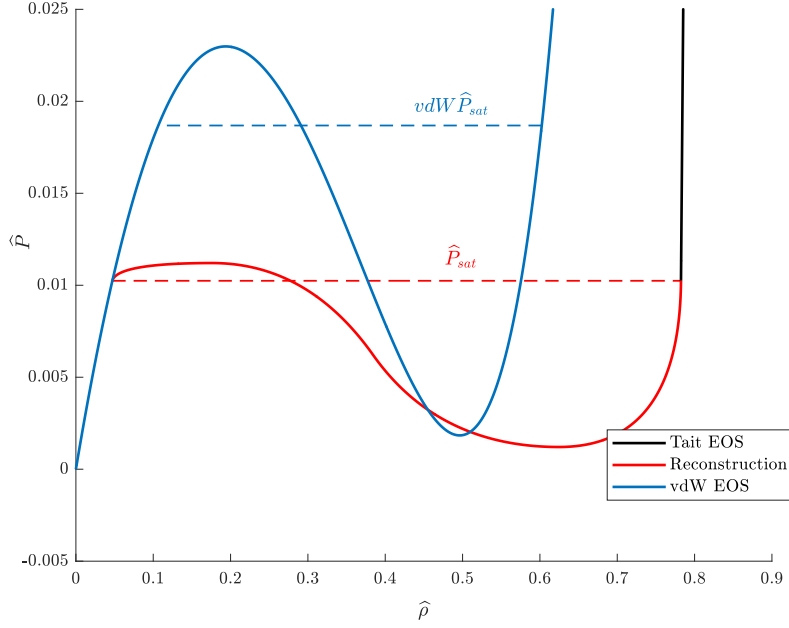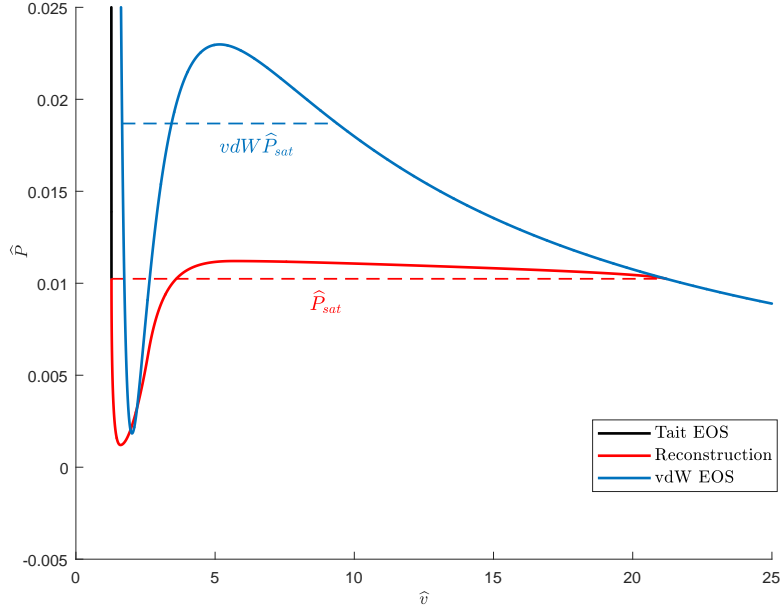
Figure 6: Equation of state for a temperature of $\widehat{T} = 0.85$. In the equation, the vapor branch is modeled with the van der Waals equation of state, and for the liquid branch we use the Modified Tait's equation. Under the saturation curve, the algorithm presented in this work is used with $\Delta P = 0.01$.

where L_0 is an arbitrary length. The numerical method includes a dimensionless characteristic length h to scale with the capillarity number, which is directly related to the width of the interface. One of the challenges that diffuse-interface models face is that, in order to be realistic, the interface must be extremely small, which would need very fine meshes to be captured [37]. In this work, following [14], the capillarity number is related with the computational mesh as

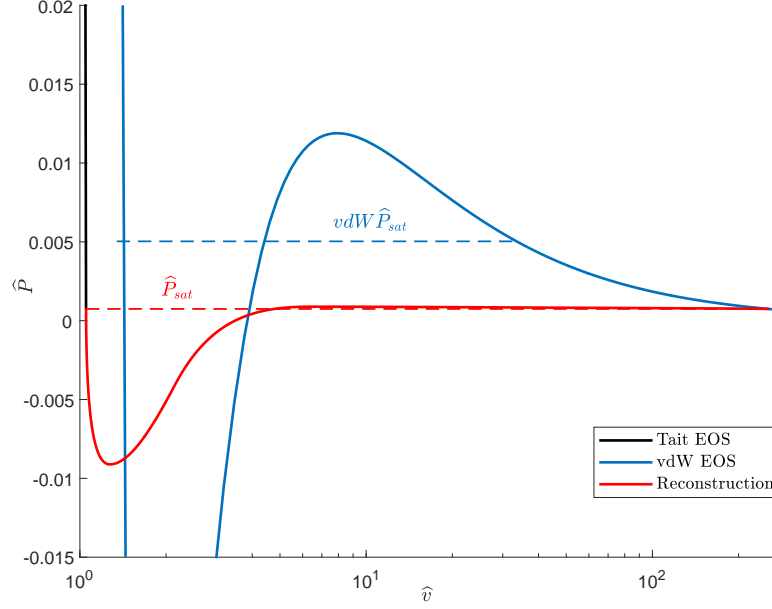$$h = \mathcal{C}\sqrt{maxA_i} \tag{17}$$

25

Figure 7: Equation of state for a temperature of $\widehat{T} = 0.85$ depending on the volume. The vapor branch of the EOS is modeled with the van der Waals equation of state, and for the liquid branch the modified Tait's equation is used. Under the saturation curve, the algorithm presented in this work is used with $\Delta P = 0.01$. The figure shows that using the proposed algorithm, the Maxwell's equal area rule is fulfilled.

where A_i is the area of the i-th element of the computational mesh. The constant parameter $\mathcal{C}$, which relates the characteristic length to the mesh, takes different values for different authors [14, 39]. Here, we set $\mathcal{C} = 1$.

Hence, in the numerical simulation of a diffuse-interface model like this, the characteristic length is a very important attribute to simulate successfully the diffuse interface. As it is shown in [39, 26], the condition that has to be accomplished is that
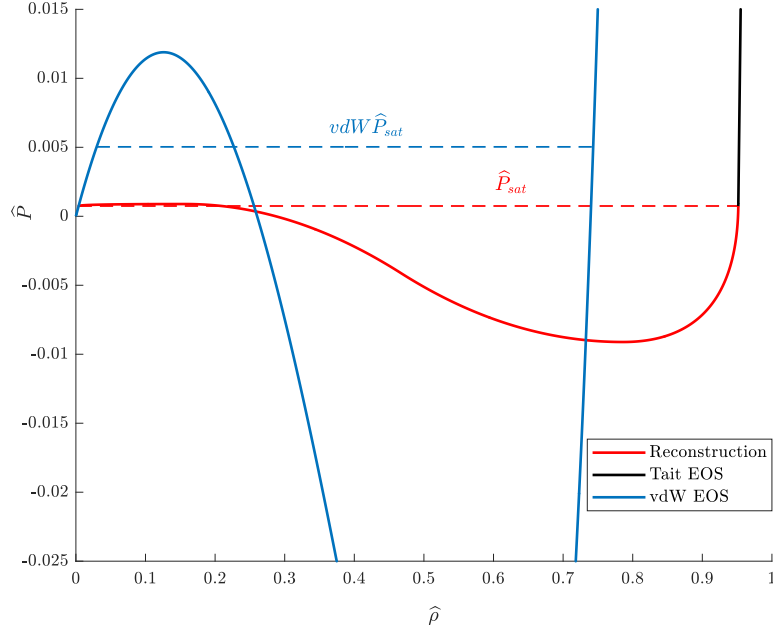
Figure 8: Equation of state obtained with the algorithm we present in this work for a temperature of $\widehat{T} = 0.65$. The vapor branch of the EOS is modeled with the van der Waals equation of state, and for the liquid branch the modified Tait's equation is used. Under the saturation curve, the algorithm presented in this work is used with $\Delta P = 0.01$.

$$h \leq \frac{\widehat{\varrho}}{\sqrt{We}}$$

This impose an upper bound to the characteristic length, where $\widehat{\varrho}$ is a dimensionless positive constant, which usually takes the value of $\widehat{\varrho} = 1$. Not accomplishing this condition may produce non-physical oscillations that do not simulate accurately the different states.

Figure 9: Equation of state for a temperature of $\widehat{T} = 0.65$ as function of the volume. The vapor branch of the EOS is modeled with the van der Waals equation of state, and for the liquid branch the modified Tait's equation is used. Under the saturation curve, the algorithm presented in this work is used with $\Delta P = 0.01$. In this figure, the volume is represented in a logarithm scale due to the large values of this variable.

4.1. Manufactured Solution

The first numerical example is the manufactured solution test case. The aim of this numerical test is to verify the accuracy of the proposed scheme in the treatment of the convective, diffusive and Korteweg-like terms. The equation to be solved is

$$\frac{\partial \rho}{\partial t} + a\frac{\partial \rho}{\partial x} - b\frac{\partial^2 \rho}{\partial x^2} + c\frac{\partial^3 \rho}{\partial x^3} = S \tag{18}$$

28

where we consider the manufactured solution

$$\rho(x,t) = \frac{1}{2}\sin(2x)\,e^{-t} \tag{19}$$

The source term S is computed by substituting the manufactured solution (19) in equation (18), to obtain

$$S(x,t) = -\frac{1}{2}e^{-t}\left(\sin(2x) - 2a\cos(2x) + 8c\cos(2x) - 4b\sin(2x)\right)$$

First, we begin with the one-dimensional test case. The computational domain is $\Omega = [0,\pi]$. Boundary conditions are prescribed using the analytical solution.. We begin with the linear convection problem, where the solution is computed with the parameters $a = 1, b = 0, c = 0$. For the pure diffusion problem we set $a = 0, b = 0.1, c = 0$ and with the Korteweg-like term $a = 0, b = 0, c = 0.01$. All the solutions are computed until $t = 0.1$. As the analytical solution is known, we can evaluate the order of accuracy of the scheme. The obtained L_2 norms of the error in ρ are shown in Table 1.

	Convection		Diffusion		Korteweg-like term	
Mesh	L2-norm	Order	L2-norm	Order	L2-norm	Order
16	1.62E-04	–	1.32E-04	–	1.58E-04	–
32	1.88E-05	3.10	3.96E-05	1.74	4.04E-05	1.97
64	2.25E-06	3.07	1.04E-05	1.93	1.03E-05	1.97
128	2.73E-07	3.04	2.63E-06	1.98	2.63E-06	1.98
256	3.37E-08	3.02	6.60E-07	1.99	6.64E-07	1.98

Table 1: 1-D Manufactured solution. Accuracy order and L2-norm of ρ for convection, diffusion and Korteweg-like behaviour.

Next, we analyze the order of convergence of the system when convective, diffusive and Korteweg-like terms take place at the same time. Two set of parameters, $a = 1, b = 0.1, c = 0.01$ and $a = 1, b = 1, c = 1$ are chosen. The obtained L_2 norms of the error in ρ are shown in Table 2.

$Mesh$	$a = 1, b = 0.1, c = 0.01$		$a = 1, b = 1, c = 1$	
	L2-norm	Order	L2-norm	Order
16	3.42E-04	–	1.41E-02	–
32	6.97E-05	2.29	3.80E-03	1.89
64	1.59E-05	2.13	9.78E-04	1.96
128	3.83E-06	2.06	2.48E-04	1.98
256	9.38E-07	2.03	6.23E-05	1.99

Table 2: 1-D Manufactured solution. Accuracy order and L2-norm of ρ for convection, diffusion and Korteweg-like behaviour.

In Tables 1 and 2 it is shown that the expected convergence rates are recovered.

In order to analyze the accuracy of our scheme on a multi-dimensional setting, we have extended this test case to 2D. The computational domain $\Omega = [0, \pi] \times [0, \pi]$ is discretized with a set of structured meshes. At the boundaries, we prescribe the analytical solution. Accuracy order and L2-norm of the error are shown in Table 3, where the expected rates are recovered.

4.2. Single bubble equilibrium

In the second example, we impose an initial condition which is not a solution of the system and we allow it to evolve until it reaches a steady state.

	$a = 1, b = 0.1, c = 0.01$		$a = 1, b = 1, c = 1$	
Mesh	L2-norm	Order	L2-norm	Order
16×16	4.72E-04	–	2.53E-02	–
32×32	7.29E-05	2.69	5.62E-03	2.17
64×64	1.72E-05	2.08	1.35E-03	2.06
128×128	4.28E-06	2.01	3.40E-04	2.02

Table 3: 2-D Manufactured solution. Accuracy order and L2-norm of ρ for convection, diffusion and Korteweg-like behaviour.

In this simulation we show the evolution of a two-dimensional vapor bubble centered in the computational domain with a fixed temperature $\widehat{T} = 0.85$. For the initial conditions, we set the radius of the bubble $R = 0.284$. The interface is shaped in the initial condition using a hyperbolic tangent profile, which is a good approximation although it does not fulfill the equation system. Additionally, the initial velocity field is set to be null. These conditions are written as follows

$$\widehat{\rho}(\boldsymbol{x}, t = 0) = 0.4148 + 0.3677 \left[tanh \left(\frac{d(\boldsymbol{x}) - R}{2h} \right) \right]$$

$$(v_x, v_y)^T = (0, 0)^T$$

where $d(\boldsymbol{x})$ is the Euclidean distance between $\boldsymbol{x}$ and the center of the computational domain $(0.5, 0.5)$. The computational mesh is composed by 64^2 elements.

In this simulation we have employed the algorithm presented in Section

31

3, with the Tait equation of state for the liquid phase, the van der Waals EOS for the vapor phase and using the reconstruction with $\Delta P = 0.01$. The result of the simulation is shown in figure 10, where we represent the steady state of the density in the two-dimensional domain. The interface separating both liquid and vapor phases is clearly seen in the figure. We also note the perfectly circular shape of the bubble, as expected.
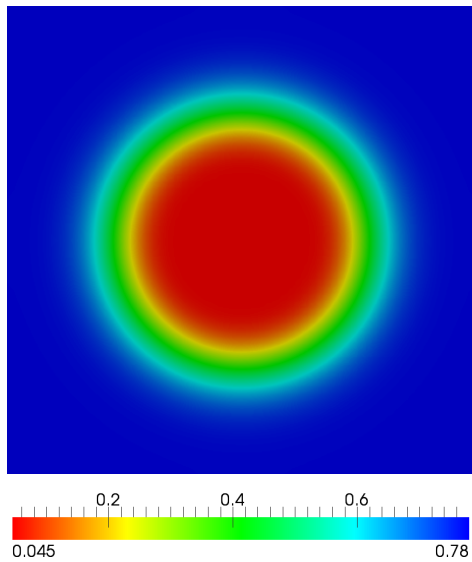

Figure 10: steady state of a single bubble immersed in liquid: Density field. For this simulation we use 64^2 elements and $\Delta t = 10^{-4}$. The EOS employed is the one plotted in figure 6.

It is important to remark that, using the algorithm presented here, for a given temperature, we are able to obtain different EOS for each value of the parameter ΔP. However, as it is pointed out in [37], changing the expression under the saturation curve will inevitably modify the underlying physics of the interface. This is addressed in the following sections.

32

4.2.1. Influence of ΔP

The equation which describes the mechanics of a vapor bubble immersed in a liquid is the Rayleight-Plesset equation [40, 41], which in the steady state is simplified to the Young-Laplace equation [42, 43].

$$\mid P_V - P_L \mid = (n-1)\sigma k \tag{20}$$

In equation (20), $\mid P_V - P_L \mid$ denotes the difference of pressure between two phases in equilibrium, which in this example are vapor and liquid. The parameter n is the number of dimensions in the problem, $k = \frac{1}{R}$ is the mean curvature of the interface and the constant σ is the surface tension. In consequence, we can rewrite the expression for this case as

$$\mid P_V - P_L \mid R = \sigma \tag{21}$$

This relation implies that for a certain temperature, we can find a value for the surface tension σ measuring the radius of the bubble in the steady state of the numerical simulations, in order to find a relation between the surface tension and the value of ΔP in our EOS algorithm. In figure 11 we plot the EOS using different values of the parameter ΔP. Note that, as all the computations are performed for the same temperature $\widehat{T} = 0.85$, the EOS for the pure phases remains unaltered, only changing the shape of the EOS under the saturation curve.

In figure 12, the steady state of the single bubble equilibrium test computed with the different EOS plotted in figure 11 is shown. A cut at $y = 0.5$ of the different density profiles obtained is displayed in figure 13. As it is seen in the figures, both the width of the interface and the radius of the bubble
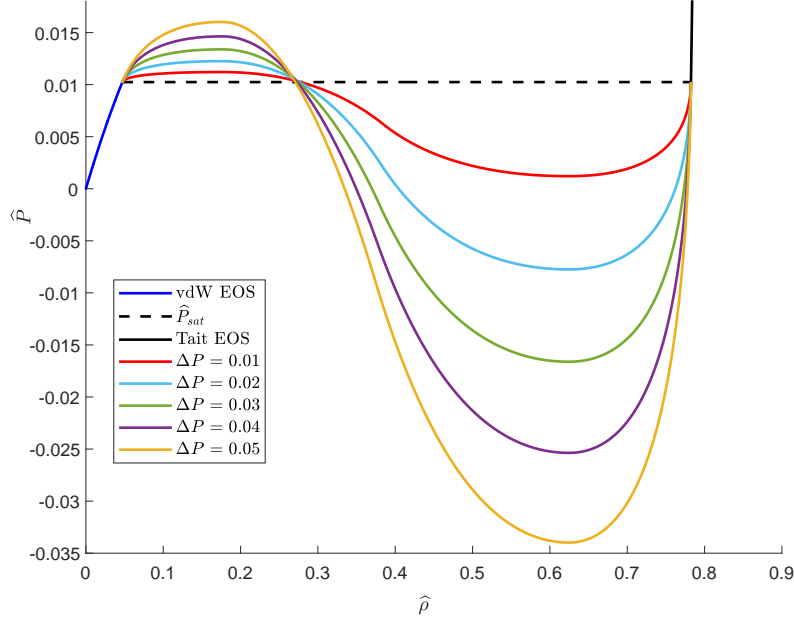
Figure 11: Representation of different EOS obtained using the algorithm proposed for the same value of temperature $\widehat{T} = 0.85$ with different values of the reconstruction parameter ΔP.

change as ΔP varies.

In order to get the radius of a bubble in a diffuse interface model, it is necessary to set a certain criterion to establish the boundary of the phases, as due to the nature of the diffuse interface models this separation remains unclear. As it is presented in [26], we define two points $\tilde{x}_1$ and $\tilde{x}_2$, which will mark the separation between the phases, as $\widehat{\rho}(\tilde{x}_1) = \widehat{\rho}(\tilde{x}_2) = (\widehat{\rho}_L - \widehat{\rho}_V)/2$ where $0 \leq \tilde{x}_1 \leq 0.5 \leq \tilde{x}_2 \leq 1$. Therefore, the boundary between the phases is located in the midpoint of the density transition. Finally, we define an approximate value of the radius as

34

(a) $\Delta P = 0.01$ (b) $\Delta P = 0.02$

(c) $\Delta P = 0.03$ (d) $\Delta P = 0.04$ (e) $\Delta P = 0.05$
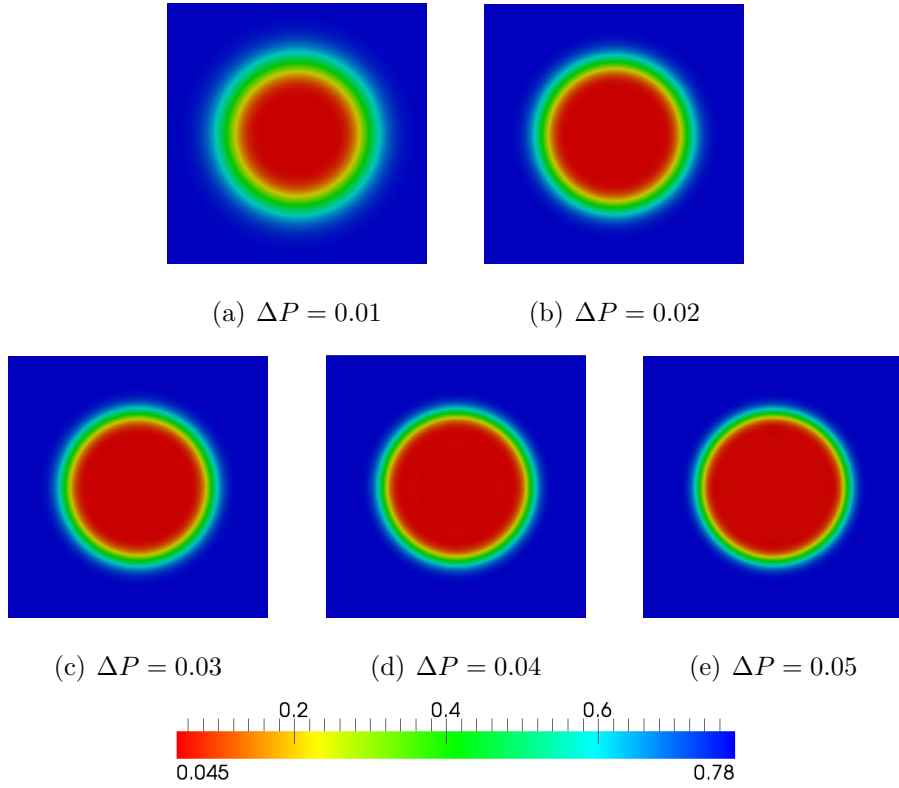
Figure 12: steady state of a single bubble immersed in liquid: Density field for different values of ΔP in the reconstruction of the EOS and a fixed temperature of $\widehat{T} = 0.85$ using the EOS plotted in figure 11. A computational mesh with 64^2 elements is used for all the computations.

$$\tilde{R} = \frac{\mid \tilde{x}_1 - \tilde{x}_2 \mid}{2}$$

Because of the nature of a numerical simulation, we are only able to obtain an approximated value of the radius $\tilde{R}$, and thus an approximated value of the surface tension $\tilde{\sigma}$, computed with the relation shown in equation (21). The values of these parameters are listed in table 4.

Another important parameter in this kind of simulations is the width of

35
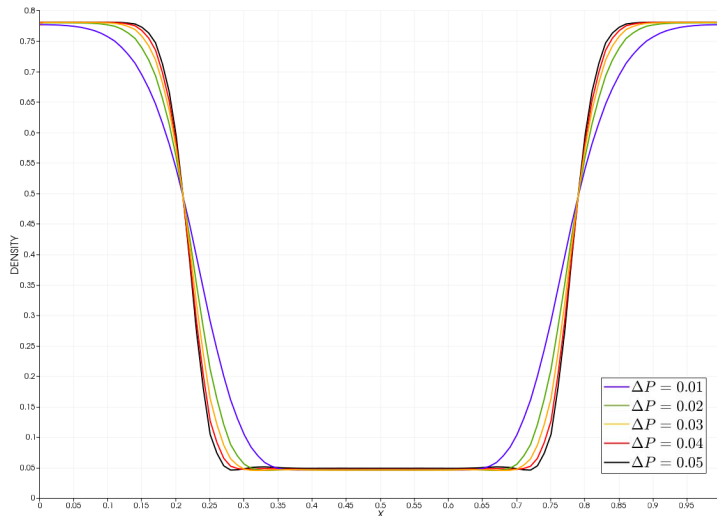
Figure 13: steady state of a single bubble immersed in liquid: Cut of the Density at $y = 0.5$ for different values of the parameter ΔP. In the examples we use the EOS plotted in figure 11. We set the same initial conditions, temperature $(\widehat{T} = 0.85)$ and a mesh composed by 64^2 elements.

the interface W. As in the case of the radius, it is necessary to establish a criterion to get this parameter from the numerical results. We set another two different points, $\widehat{x}_1$ and $\widehat{x}_2$, such as $\widehat{\rho}(\tilde{x}_1) = \widehat{\rho}_L - 0.05(\widehat{\rho}_L - \widehat{\rho}_V)$ and $\widehat{\rho}(\tilde{x}_2) = \widehat{\rho}_V + 0.05(\widehat{\rho}_L - \widehat{\rho}_V)$, with $0 \leq \tilde{x}_1 \leq \tilde{x}_2 \leq 0.5$. By choosing these points, we ensure that the 90% of the variation is produced within the interface. Hence, we define an approximate value of the interface width as

$$\tilde{W} = \mid \tilde{x}_1 - \tilde{x}_2 \mid$$

The variation of $\tilde{W}$ depending on ΔP is also listed in table 4.

In table 4 it is shown that the approximated surface tension $\tilde{\sigma}$ increases with the parameter ΔP. As when $\Delta P \to 0$, then $\tilde{\sigma} \to 0$, we find that the

$\widehat{T}$	ΔP	$\tilde{R}$	$\tilde{W}$	$|\widehat{P}_V - \widehat{P}_L|$	$\tilde{\sigma}$
0.85	0.05	0.2823	8.537×10^{-2}	5.534×10^{-3}	1.562×10^{-3}
	0.04	0.2817	9.747×10^{-2}	4.908×10^{-3}	1.383×10^{-3}
	0.03	0.2801	11.30×10^{-2}	4.234×10^{-3}	1.186×10^{-3}
	0.02	0.2781	13.59×10^{-2}	3.491×10^{-3}	0.9707×10^{-3}
	0.01	0.2722	19.12×10^{-2}	2.481×10^{-3}	0.6752×10^{-3}

Table 4: Approximated data from the numerical examples of a single bubble in equilibrium. The numerical simulations are computed with the same temperature $\widehat{T} = 0.85$ and a time step of $\Delta t = 10^{-4}$. In this table we show the relation between the radius of the bubble $\tilde{R}$, the width of the interface $\tilde{W}$ and the surface tension $\tilde{\sigma}$ with the parameter of the reconstruction proposed ΔP.

relation between the surface tension and the parameter ΔP, for $\widehat{T} = 0.85$, can be accurately approximated with a square root function, as

$$\tilde{\sigma} = 0.0069\sqrt{\Delta P} \tag{22}$$

as it is shown in figure 14.

Conceptually, higher values of the surface tension can hold bubbles with larger radii. In the limit with no surface tension the bubble is not stable under the pressure the liquid imposes.

In table 4 it is also shown that the parameter ΔP has also an influence on the width of the interface. This fact was already addressed in [37], where the author proposes a method to enlarge the interface by reducing drastically the difference of pressure between the spinodal points. From the data shown in figure 14, we find that the relation between the width of the interface $\tilde{W}$
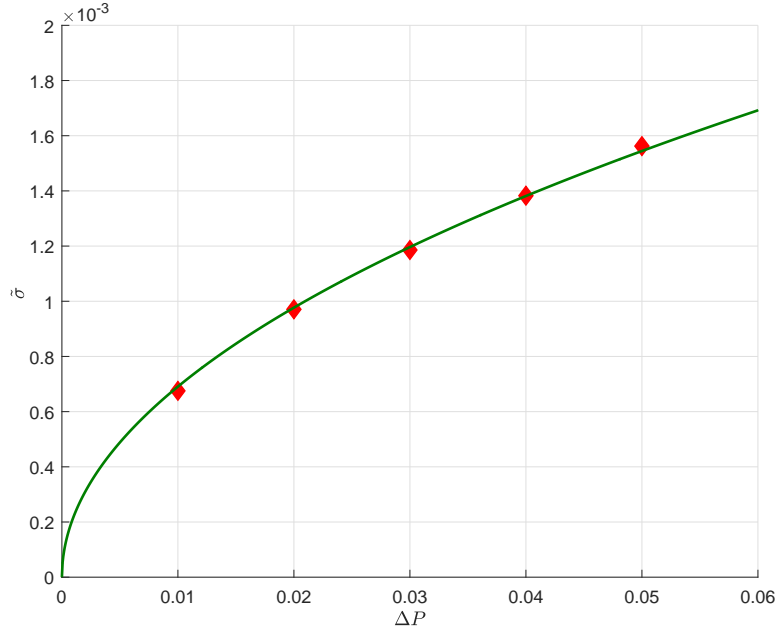
Figure 14: Relation between the reconstruction parameter ΔP and the approximated value of the surface tension $\tilde{\sigma}$ for $\widehat{T} = 0.85$ and a mesh composed by 64^2 elements. The straight line is the curve obtained using equation (22) and the red diamonds are the results obtained from the numerical simulations.

and ΔP, for $\widehat{T} = 0.85$, can be approximated as

$$\tilde{W} = 0.0193/\sqrt{\Delta P} \tag{23}$$

as it is shown in figure 15.

Note that relations (22) and (23) are obtained empirically for a very specific case, and thus this relations may change for other problems.
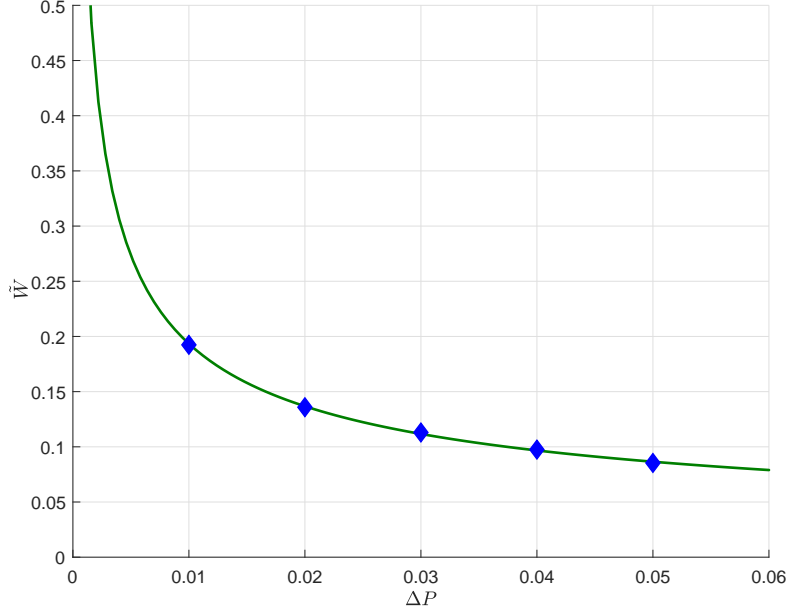
Figure 15: Relation between the reconstruction parameter ΔP and the approximated value of the interface thickness $\tilde{W}$ for $\widehat{T} = 0.85$ and a mesh composed by 64^2 elements. The straight line is the curve obtained using equation (23) and the blue diamonds are the results obtained from the numerical simulations.

4.2.2. Influence of the characteristic length

For the numerical method to be precise, it needs a thin and therefore realistic representation of the interface [37]. On the other hand, if the mesh is not fine enough to capture the interface, non-wanted oscillations may appear in the solution and affect its accuracy. Although we have seen that the parameter ΔP has an influence on the width of the interface, the method includes a characteristic length h (see equations (16) and (17)) to adapt the interface to the mesh. However, the characteristic length will also affect the predicted value of the surface tension.

39

In order to study the relation between the surface tension and h, we have performed several simulations with the same temperature and the same ΔP. The objective of this study is to find a combined equation which relates the surface tension to both h and ΔP for the isothermal version of the method. With simulations for meshes composed by 32^2, 48^2, 64^2, 96^2 and 128^2 elements, related with h through (17), for $\widehat{T} = 0.85$ we can accurately approximate the surface tension as

$$\tilde{\sigma} = 0.4442h\sqrt{\Delta P} \tag{24}$$

as it is shown in figure 16.
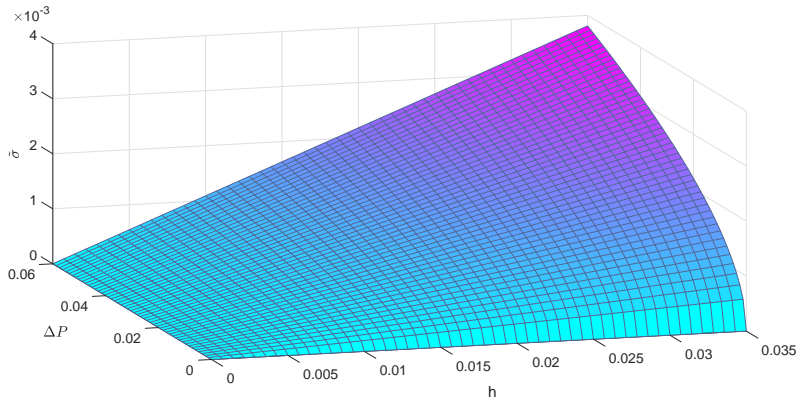
Figure 16: Relation between surface tension and the reconstruction parameter ΔP and the characteristic length of the mesh h. In the figure it is seen that the surface tension increases linearly with h and has a relation with ΔP of a square root function.

Figure 16 shows empirically that the surface tension increases linearly with the characteristic length and has the same relation with ΔP that we have shown in figure 14. These relations are in agreement with the results presented in [37]. Finally, analogously to the study performed for the surface

tension, we find the relation of ΔP and h with the thickness of the interface $\tilde{W}$. We find that

$$\tilde{W} = 1.278h/\sqrt{\Delta P} \tag{25}$$
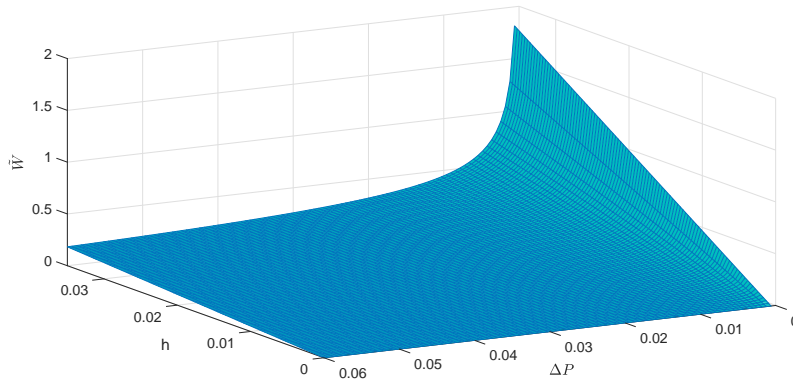
This relation is shown in figure 17.

Figure 17: Relation between the thickness of the interface and the reconstruction parameter ΔP and the characteristic length of the mesh h. In the figure it is seen that the surface tension increases linearly with h and has a relation with ΔP of an inverse square root function.

Note that in a numerical simulation, one of the most important factors is the size of the mesh. For the practical application of the methodology presented in this work, we propose to select a suitable mesh and then select the reconstruction parameter ΔP in order to obtain the desired value of the surface tension using equation (24). Once h and ΔP are selected, the width of the interface is established automatically. It is important to remark that this have some consequences on the underlying physics that the method is able to represent, as presented in [37].

Note that relations (24) and (25) are obtained empirically for a very

specific case, and thus this relations may change for other problems.

4.2.3. Effects of temperature

According to equations (24) and (25), low values of the characteristic length h or great values of ΔP lead to thinner interfaces and therefore to the need of finer meshes. For example, in figure 13 it is seen that for the highest value of ΔP ($\Delta P = 0.05$) a slight oscillations occurs. This is a well-known problem with numerical simulations using the van der Waals equation of state, where the difference of pressure between the spinodal points creates very thin interfaces difficult to capture by the mesh, a problem which grows exponentially when the temperature decreases. With the method proposed in this work, we are able to control the expression of the EOS under the saturation curve, and therefore we can partially solve this problem, being able to perform numerical simulations with lower temperatures. In figure 8, it is seen that for a lower value of the temperature ($\widehat{T} = 0.65$), the difference of pressure of the spinodal points increases exponentially in the van der Waals EOS, whereas using the proposed method we are able to control this attribute.

To analyze the effects of temperature variations, we show in figure 18 the density profile of the numerical simulation of the single bubble equilibrium for different values of the temperature and the same $\Delta P = 0.01$ with the same computational mesh with 64^2. As in the previous subsections, different values of the parameters are collected in table 5. It is appreciated that, although the interface width grows when the temperature drops, decreasing the value of the temperature may produce non-wanted oscillations. In figure 18 for $\widehat{T} = 0.65$, in spite of having a wider interface, slight oscillations in the

density appear.
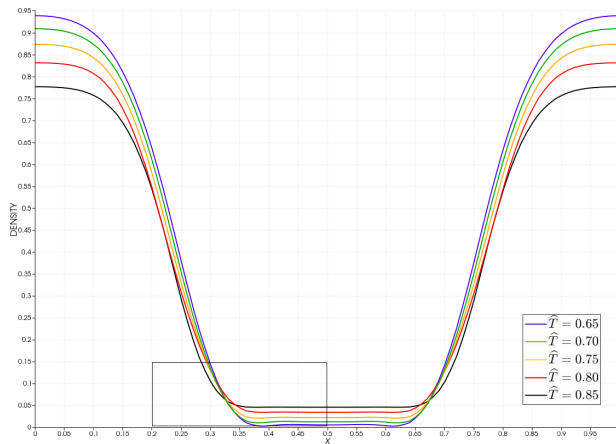
(a)
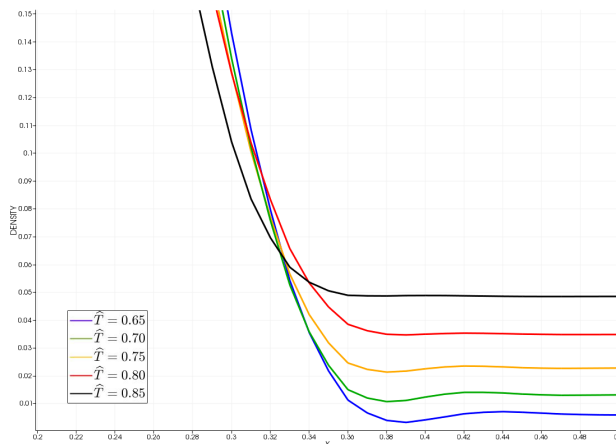
(b)

Figure 18: Single bubble problem: In (a), we show we show a cut of the density at $y = 0.5$ for different values of the temperature. For this examples we use the same value of the reconstruction parameter ΔP and the time step $\Delta t = 10^{-5}$. In (b), we show a zoom of the rectangle marked in (a).

This problem is usually soften by refining the grid, searching for a more accurate discretization. With the proposed algorithm, we manage to elimi-

$\widehat{T}$	ΔP	$\tilde{R}$	$\tilde{W}$	$|\widehat{P}_V - \widehat{P}_L|$	$\tilde{\sigma}$
0.85	0.01	0.2725	0.1888	2.996×10^{-3}	0.8164×10^{-3}
0.80	0.01	0.2767	0.2003	3.104×10^{-3}	8.590×10^{-3}
0.75	0.01	0.2737	0.2148	3.639×10^{-3}	9.962×10^{-3}
0.70	0.01	0.2706	0.2198	4.139×10^{-3}	1.120×10^{-3}
0.65	0.01	0.2675	0.2255	4.622×10^{-3}	1.236×10^{-3}

Table 5: Approximated data obtained from the numerical simulation of a single bubble immersed in a liquid. In this table we represent the relation between the radius of the bubble $\tilde{R}$, the width of the interface $\tilde{W}$ and the surface tension $\tilde{\sigma}$ with the temperature $\widehat{T}$. For the simulation, the parameter of the interpolation ΔP is remained constant and the time step employed is $\Delta t = 10^{-5}$.

nate to a great extent the dependence on the mesh by adjusting the value of the parameter ΔP. By reducing the value of ΔP we are able to achieve numerical solutions at lower temperatures, taking into account that decreasing ΔP makes the interface become wider and also reduces the surface tension σ.

In figure 19 we show a numerical simulation of the single bubble equilibrium with different sizes of the mesh (and thus different values of h, equation (17)) and different values of the parameter ΔP at $\widehat{T} = 0.80$. For a computational mesh composed by 64^2 elements and $\Delta P = 0.03$, spurious oscillations are produced. As shown in the figure, making ΔP smaller can reduce the oscillations to the same magnitude as reducing the value of h using more elements in the mesh.
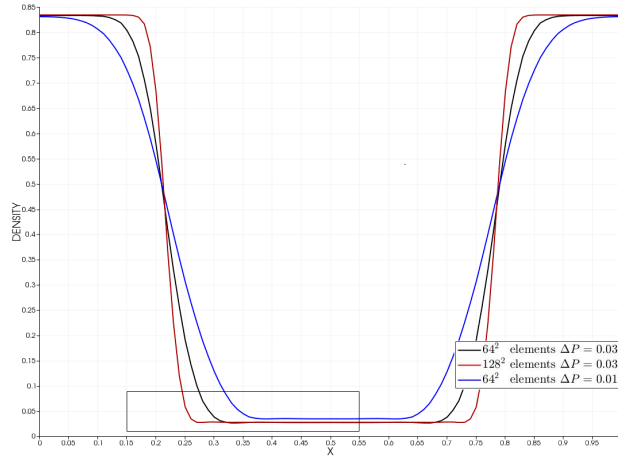
(a)
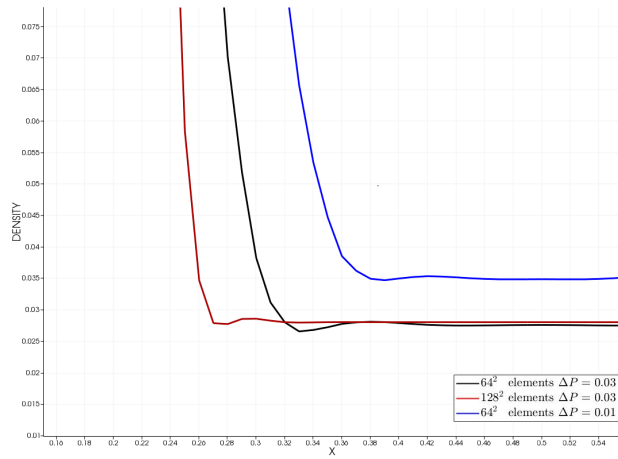
(b)

Figure 19: Single bubble problem: In (a), we show a cut of the density at $y = 0.5$ for a temperature $\widehat{T} = 0.80$, using a mesh composed by 64^2 and 128^2 elements and the EOS computed with $\Delta P = 0.03$ and $\Delta P = 0.01$. In (b) we show a zoomed view of the rectangle marked in (a). Spurious oscillations that appear in the simulation with a mesh of 64^2 elements and $\Delta P = 0.03$ can be soften not only using a thinner mesh, like the one we plot with 128^2 elements, but also adapting the value of ΔP.

4.3. Coalescence of two bubbles

In the previous examples, a solitary bubble grew or shrank until it arrived to the steady state. With two or more bubbles sharing the same space, the smaller bubbles will collapse due to the great pressure larger bubbles impose. When the vapor bubbles are close enough (a distance in the same order of magnitude of the thickness of the interface), they will merge to form a lonely and larger bubble which will evolve to a circular shape [14]. To simulate this phenomenon of coalescence, we will place two vapor bubbles in the computational domain Ω. Their centers are placed at $O_1 = (0.375, 0.5)$ and $O_2 = (0.775, 0.5)$. Their radii are $R_1 = 0.25$ and $R_2 = 0.10$ respectively. The initial condition is establish as in the previous examples using a hyperbolic tangent profile to model the interfaces, and it reads as

$$\widehat{\rho}(\boldsymbol{x}, t = 0) = 0.04718 + 0.3676 \left[tanh\left(\frac{d_1(\boldsymbol{x}) - R_1}{2h}\right) + tanh\left(\frac{d_2(\boldsymbol{x}) - R_2}{2h}\right) \right]$$

$$(v_x, v_y)^T = (0, 0)^T$$

where $d_i(\boldsymbol{x})$ is the Euclidean distance between $\boldsymbol{x}$ and O_i, with $i = 1, 2$. The computational domain is discretized using both a 128^2 and a 256^2 grid. In figures 20 and 21 the evolution of the density and pressure fields in time are shown using a computational mesh composed by 256^2 elements. These figures show the ability of the numerical method to reproduce abrupt variations in the topology of the problem. The results obtained using the proposed methodology are in agreement with those of [14].

According to the Young-Laplace equation (20), the difference in pressure between vapor and liquid phases is inversely proportional to the radius of
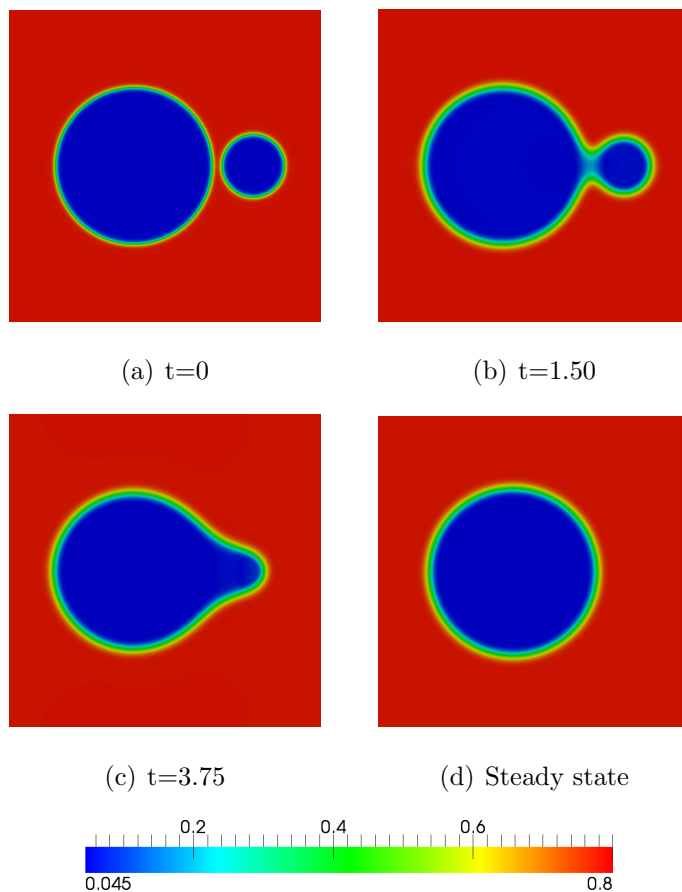
46

(a) t=0   (b) t=1.50

(c) t=3.75   (d) Steady state

Figure 20: Coalescence of two bubbles: Evolution of the density field. Results on a 256^2 grid.

the bubble. As σ is a constant parameter only depending on the equation of state and the capillarity number, we can establish a relation with the approximated surface tension $\tilde{\sigma}$ calculated in the coalescence example and the single bubble equilibrium as

$$\mid \widehat{P}_V - \widehat{P}_L \mid_1 R_1 = \mid \widehat{P}_V - \widehat{P}_L \mid_2 R_2$$

47
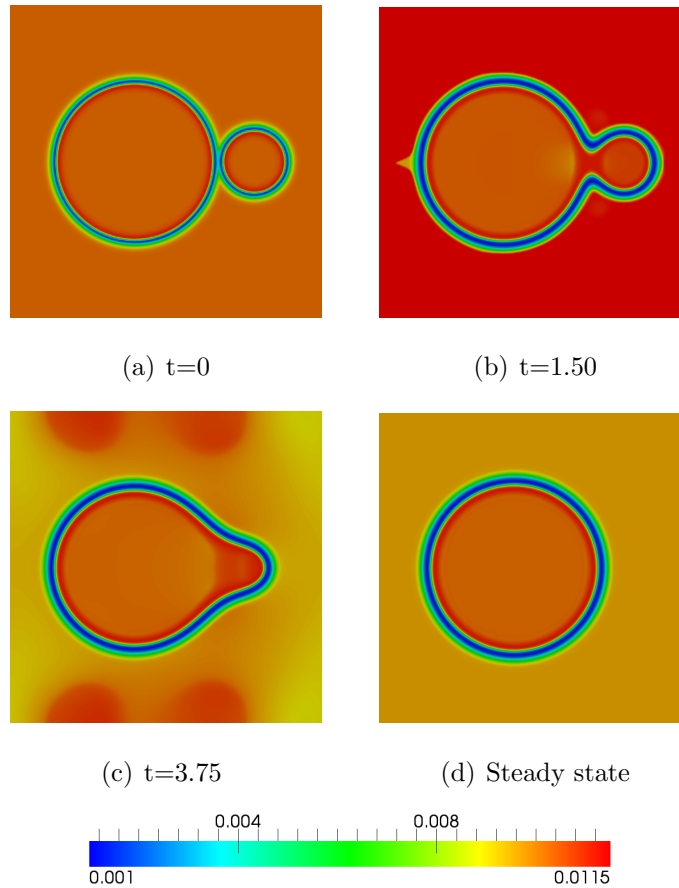
Figure 21: Coalescence of two bubbles: Evolution of the pressure field. Results on a 256^2 grid.

where the sub-index 1 and 2 refer to two different examples with the same EOS. In order to find the error of the numerical solution, we check if the results verify the Young-Laplace equation by simulating the coalescence of the bubbles with the same conditions that the single bubble equilibrium. For $\widehat{T} = 0.85$, $\Delta P = 0.01$ and a mesh composed by 128^2 elements:

$$| \widehat{P}_V - \widehat{P}_L |_1 \simeq 1.220 \times 10^{-3} \quad \tilde{R}_1 \simeq 0.2805$$

$$| \widehat{P}_V - \widehat{P}_L |_2 \simeq 1.287 \times 10^{-3} \quad \tilde{R}_2 \simeq 0.2684$$

which implies that, for this conditions, the Young-Laplace equation is verified with a relative error of 9.62×10^{-3}.

Conclusions

In this work we have proposed a new high-order accurate finite volume formulation for the resolution of Navier-Stokes Korteweg equations, based on the Moving Least Squares (MLS) approximations. The Moving Least Squares approach is employed in order to obtain high-order approximations and derivatives which allow us to obtain a high-order numerical method in both structured and non-structured meshes.

Moreover, we have presented a new algorithm to obtain more precise equations of state. In this method, we use more accurate equations of state in pure phases joined together using a B-Spline reconstruction, creating new expressions of the equation of state under the saturation curve. The main advantage of this algorithm is the ease of its application and his versatility, since to be used is only necessary the saturation points and the slopes of the equation of states. Besides, although in this work we apply this algorithm to the specific case of water, it can be used for a great range of substances as well.

Finally, we have shown some numerical examples of the formulation, where we manifest the robustness of the method. In this examples, we find

empirically a relation between the parameters used in the interpolation and important variables in the numerical calculus, such as the radius of the bubble, the width of the interface and the surface tension. Having the control of the expression under the saturation curve allows us to select previously desirable values for this variables. Furthermore, using the algorithm proposed also allows us to soften the dependence on the mesh of the numerical simulations.

Acknowledgments

References

[1] *Batchelor, G.K.,* An Introduction to Fluid Dynamics, *Cambridge University Press, 1967.*

[2] *Crank, J.,* Free and Moving Boundary Problems, *Oxford University Press, 1997.*

[3] Lighthill, J., Waves in Fluids, *Cambridge University Press, 1978.*

[4] Anderson, D.M., McFadden, G.B., Wheeler, A.A., Diffuse-interface methods in fluid mechanics, *Annual Review of fluid Mechanics, 30:139–165, 1998.*

[5] Garcke, H., Novick-Cohen, A., A singular limit for a system of degenerate Cahn-Hilliard equations, *Adv Differential Equations, 5:401–434, 2000.*

[6] Garcke, H., Nestler, B., A mathematical model for grain growth in thin metallic films, *Mathematical Models Methods Applied Science, 10:895–921, 2000.*

[7] Garcke, H., Nestler, B., Stoth, B., On anisotropic order parameter models for multiphase systems and their sharp interface limits, *Phys D, 115:87–108, 1998.*

[8] Korteweg, D.J., Sur la forme que prennent les équations du mouvements des fluides si l'on tient compte des forces capillaires causées par des variations de densité consiérables mais continues et sur la théorie de la capillarité dans l'hypothèse d'une variation continue de la densité, *Archives Néerlandaises des Sciences Exactes et Naturelles. Series II, 6:1–24, 1901.*

[9] Jamet, D., Torres, D., Brackbill, J.U., On the theory and computation of surface tension: the elimination of parasitic currents through energy conservation in the second-gradient method, *Journal of Computational Physics, 182:262–276, 2002.*

[10] Diehl, D., Higher Order Schemes for Simulation of Compressible Liquid-Vapor Flows with Phase Change, *PhD Thesis, 2007.*

[11] *Diehl, D., Kremser, J., Kröner, D., Rohde, C.,* Numerical solution of Navier–Stokes-Korteweg systems by Local Discontinuous Galerkin methods in multiple space dimensions, *Applied Mathematics and Computation, 272:309-335, 2016.*

[12] *Tian, L., Xu, Y., Kuerten, J. G. M., van der Vegt, J. J. W.,* An h-adaptive local discontinuous Galerkin method for the Navier–Stokes–Korteweg equations *Journal of Computational Physics, 319:266-279, 2016.*

[13] *Neusser, J., Rohde, C., Schleper, V.,* Relaxation of the Navier–Stokes–Korteweg equations for compressible two-phase flow with phase transition *International Journal for Numerical Methods Fluids, 79(12):615-639, 2015.*

[14] *Gómez, H., Hughes, T.J.R., Nogueira, X., Calo, V.C.,* Isogeometric analysis of the isothermal Navier-Stokes-Korteweg equations, *Computer Methods in Applied Mechanics and Engineering, 199:1828–1840, 2010.*

[15] *Cueto-Felgueroso, L., Colominas, I., Fe, J., Navarrina, F., Casteleiro, M.,* High order finite volume schemes on unstructured grids using Moving Least Squares construction. Application to shallow waters dynamics, *International Journal for Numerical Methods in Engineering, 65:295–331, 2006.*

[16] *Cueto-Felgueroso, L., Colominas, I., Nogueira, X., Navarrina, F., Casteleiro, M.,* Finite volume solvers and Moving Least-Squares approximations for the compressible Navier-Stokes equations on unstruc-

tured grids, *Computer Methods in Applied Mechanics and Engineering*, *196:4712–4736, 2007.*

[17] *Cueto-Felgueroso, L., Colominas, I.,* High-order finite volume methods and multiresolution reproducing kernels, *Archives of Computational Methods in Engineering, 15 (2):185–228, 2008.*

[18] *Khelladi, S., Nogueira, X., Bakir, F., Colominas, I.,* Toward a higher order unsteady finite volume solver based on reproducing kernel methods, *Computer Methods in Applied Mechanics and Engineering, 200(29):2348–2362, 2011.*

[19] *Nogueira, X., Ramírez, L., Khelladi, S., Chassaing, J., Colominas, I.,* A high-order density-based finite volume method for the computation of all-speed flows, *Computer Methods in Applied Mechanics and Engineering, 298:229–251, 2015.*

[20] *Lancaster, P., Salkauskas, K.,* Surfaces generated by moving least squares methods, *Mathematics of Computation, 37 (155):141–158, 1981.*

[21] *Gossler, A.,* Moving Least-Squares:a numerical differentiation method for irregulary spaced calculation points, *SANDIA Report, SAND2001-1669, 2001.*

[22] *Li, S., Liu, W.K.,* Moving least squares reproducing kernel method part II: Fourier Analysis, *Computer Methods in Applied Mechanics and Engineering, 139 159–193, 1996.*

[23] *Liu, W.K., Li, S., Belytschko, T.,* Moving least squares reproducing

kernel method part I: Methodology and convergence, *Computer Methods in Applied Mechanics and Engineering, 143 113–154, 1997.*

[24] *van der Waals, J.D.,* On the continuity of the Gaseous and Liquid States, *PhD Thesis, 1873.*

[25] *van der Waals, J.D.,* The thermodynamic theory of capillarity under the hypothesis of a continuous variation of density, *Journal of Statistical Physics (Reprinted), 20:197–244, 1979.*

[26] *Liu, J., Landis,C.M., Gómez, H., Hughes, T.J.R.,* Liquid-vapor phase transition: Thermomechanichal theory, entropy stable numerical formulation, and boiling simulations, *Computer Methods in Applied Mechanics and Engineering, 297:476–553, 2015.*

[27] *Rusanov, V. V.,* The calculation of the interaction of non-stationary shock waves and obstacles, *USSR Computational Mathematics and Mathematical Physics, 1(2):304-320, 1962.*

[28] *Li, X.-S, Gu, C.-W,* Mechanism of Roe-type schemes for all-speed flows and its application, *Computers and Fluids, 86:56-70, 2013.*

[29] *Nogueira, X., Cueto-Felgueroso, L., Colominas, I., Gómez, H., Navarrina, F. and Casteleiro, M.,*On the accuracy of finite volume and discontinuous Galerkin discretizations for compressible flow on unstructured grids, *International Journal for Numerical MEthods in Engineering, 78:1553-1584, 2009.*

[30] *Tait, P.G.,* Report on some of the physical properties of fresh water and of sea water, *Physics and chemistry, 35:1–76, 1888.*

[31] *Li, Y.H.,* Equation of state of water and sea water, *Journal of Geophysical Research, 72:2665–2678, 1967.*

[32] *National Institute of Standards and Technology. Thermophysical Properties of Fluid Systems. http://webbook.nist.gov/chemistry/fluid/, 2012. [Online; access June 13th 2017].*

[33] *Kupershtokh, A.L.,* A lattice Boltzmann equation method for real fluids with the equation of state known in tabular form only in regions of liquid and vapor phases, *Applied Mathematics and Computation, 61:3537–3548, 2011.*

[34] *Serrin, J.,* The Area Rule for Simple Fluid Phase Transitions, *Journal of Elasticity, 90:129–159, 2008.*

[35] *Dunn, J.E., Serrin, J.,* On the thermomechanics of interstitial working, *Archives for Rational Mechanics and Analysis, 88:95–133, 1985.*

[36] *Gibbs, J.W.,* On the Equilibrium of Heterogeneous Substances, *Transactions of the Connecticut Academy of Arts and Sciences, 3:108–248, 1875.*

[37] *Jamet, D., Lebaigue, O., Coutris, N., Delhaye, J.M.,* The Second Gradient Method for the Direct Numerical Simulation of Liquid–Vapor Flows with Phase Change, *Journal of Computational Physics, 169:624–651, 2001.*

[38] *De Boor, C.,* On Calculating with B-Splines, *Journal of Approximation Theory, 6:50–62, 1972.*

[39] Liu, J., Gómez, H., Evans, J.A., Hughes, T.J.R., Landis, C.M., Functional entropy variables: A new methodology for deriving thermodynamically consistent algorithms for complex fluids, with particular reference to the isotermal Navier-Stokes-Korteweg equations, *Journal of Computational Physics, 248:47–86, 2013.*

[40] Rayleight, L., On the pressure developed in a liquid during the collapse of a spherical cavity, *Philosophical Magazine, 34(200):94–98, 1917.*

[41] Plesset, M.S., The Dynamics of Cavitation Bubbles, *Journal of Applied Mechanics, 16:228–231, 1949.*

[42] Young, T., An essay on the cohesion of fluids, *Philosophical Transactions of the Royal Society of London, 95:65–87, 1805.*

[43] Laplace, P.S, Traité de Mécanique Céleste: Tome IV, *Supplément au dixième livre du Traité de Mécanique Céleste, 1–79, 1805.*